Article

Assessing the Added Value of Sentinel-1 PolSAR Data for Crop Classification

Maria Ioannidou [1,†], Alkiviadis Koukos [1,*,†], Vasileios Sitokonstantinou [1], Ioannis Papoutsis [2] and Charalampos Kontoes [1]

1   BEYOND Center, IAASARS, National Observatory of Athens, 15236 Penteli, Greece
2   Orion Lab, IAASARS, National Observatory of Athens, 15236 Penteli, Greece
*   Correspondence: akoukos@noa.gr
†   These authors contributed equally to this work.

Abstract: Crop classification is an important remote sensing task with many applications, e.g., food security monitoring, ecosystem service mapping, climate change impact assessment, etc. This work focuses on mapping 10 crop types at the field level in an agricultural region located in the Spanish province of Navarre. For this, multi-temporal Synthetic Aperture Radar Polarimetric (PolSAR) Sentinel-1 imagery and multi-spectral Sentinel-2 data were jointly used. We applied the Cloude–Pottier polarimetric decomposition on PolSAR data to compute 23 polarimetric indicators and extracted vegetation indices from Sentinel-2 time-series to generate a big feature space of 818 features. In order to assess the relevance of the different features for the crop mapping task, we run a number of scenarios using a Support Vector Machines (SVM) classifier. The model that was trained using only the polarimetric data demonstrates a very promising performance, achieving an overall accuracy over 82%. A genetic algorithm was also implemented as a feature selection method for deriving an optimal feature subset. To showcase the positive effect of using polarimetric data over areas suffering from cloud coverage, we contaminated the original Sentinel-2 time-series with simulated cloud masks. By incorporating the genetic algorithm, we derived a high informative feature subset of 120 optical and polarimetric features, as the corresponding classification model increased the overall accuracy by 5% compared to the model trained only with Sentinel-2 features. The feature importance analysis indicated that apart from the Sentinel-2 spectral bands and vegetation indices, several polarimetric parameters, such as Shannon entropy, second eigenvalue and normalised Shannon entropy are of high value in identifying crops. In summary, the findings of our study highlight the significant contribution of Sentinel-1 PolSAR data in crop classification in areas with frequent cloud coverage and the effectiveness of the genetic algorithm in discovering the most informative features.

Keywords: crop type mapping; time series; cloud cover; genetic algorithm; feature selection; radar polarimetry; common agricultural policy

1. Introduction

Over recent decades, the continuous population growth, climate change, and scarcity of arable land have raised several challenges with regards to ensuring food security, conserving natural habitat and resources, as well as maintaining economic and social stability. Considering the complexity and seriousness of the above issues, cropland and crop type mapping are of utmost relevance [1,2]. Timely and accurate remote classification of crops can support the monitoring and management of agricultural fields, the effective spatial allocation of agricultural practices and crops, and of course the large-scale prediction of yield [3–5]. The traditional way of manually documenting fields' crop type, extent and location is by carrying out on-the-spot field investigations, which requires a considerable amount of human resources, time, money, and labor [6]. Nowadays, the use of Earth

Observation (EO) data acquired from increasingly improving space-borne remote sensing technologies, and the extended application of artificial intelligence techniques in monitoring and mapping crops offer practical and cost-effective solutions as an alternative to field visits [7].

The practical benefits of remotely detecting the type and status of crops are highlighted in the context of European's Union (EU) Common Agricultural Policy's (CAP) scheme. CAP is an initiative for supporting agricultural activities of European countries and providing subsidies, according to farmers' declarations about the location, area, and type of their cultivated fields [8]. European Commission has recently enacted several legal reforms for enabling the use of EU's Copernicus Sentinel-1 and Sentinel-2 satellite data, in order to optimize CAP's activities and to ensure farmers' compliance to CAP rules [9]. Each one of Sentinel-1 and Sentinel-2 missions was designed as a two-satellite constellation that acquire C-band radar and optical satellite images of Earth, respectively. Sentinel images are freely available [10,11], providing great opportunities for cost-effective research and application development in a variety of remote sensing domains. Additionally, the high temporal, spatial, and spectral resolution of the collected data, combined with the wide area and global coverage provided [12], render Sentinel satellites an extremely attractive option, specifically, for effective monitoring of agricultural land and the production of high-quality crop maps [13].

According to the scientific literature of recent decades, building crop classification models using optical imagery as input data is one of the most popular approaches [14]. Optical images are constructed based on plants' spectral responses in different wavelengths of the ultraviolet, visible, and infrared part of the spectrum [15] and contain rich information about vegetation's status and biophysical properties [3,16]. As mentioned earlier, Sentinel-2 satellites provide freely available images of high spatial, spectral, and temporal characteristics and their great potential in accurate crop type mapping has been demonstrated by many studies [17–24].

Although optical remote sensing systems offer numerous benefits for extracting valuable knowledge and implementing effective innovative solutions in crop classification research tasks, such systems suffer from an important limitation: the collection of clear, usable images depends on the atmospheric or weather conditions and, as a result, frequent cloud cover over an area of interest can render its monitoring challenging or unfeasible [25]. As opposed to the optical systems, satellite missions that are equipped with Synthetic Aperture Radar (SAR) sensors can acquire images day or night and under all-weather conditions [26], being an extremely valuable source of information for mapping agricultural fields in countries with frequent rain and cloud cover [27]. Additionally, backscattering signals of transmitted microwaves are sensitive to the geometric, structural, and dielectric properties of plants and soil [28], rendering SAR data very useful for effectively discriminating different types of vegetation cover. Since its launch, the Sentinel-1 mission has gained increasing attention by the remote sensing community thanks to its great capabilities, such as its short revisit time, high spatial resolution, dual polarization system, and open access policy. Specifically, many researchers have evaluated the potential of Sentinel-1 data in distinguishing different crop types and, in many cases, its contribution to accurate crop classification has been highlighted [9,29,30]. For example, refs. [29] and [9] both used Sentinel-1 VV and VH backscatter time-series for identifying tens of different crop types, achieving very promising results with overall accuracy of more than 70% and 88%, respectively. Ref. [30] used time-series of both Sentinel-1 coherence and backscattering coefficients to classify 17 crop types in Sevilla, Spain, and achieved an overall accuracy of more than 86%. At this point, it is worth mentioning that the majority of crop classification studies, making use of Sentinel-1 imagery, follow the typical approach of incorporating, as input data, only the backscatter intensity information in different polarization channels, while ignoring information about the phase changes of the microwave radiation. For more details on studies for crop classification using SAR data, in [2,26] the authors present detailed review analyses and in the recent work of [31] the authors have carried out an extensive

review of deep learning applications on SAR data, which highlights the trend so far, as well as the future research directions.

Compared to SAR data, containing information only for the amplitude of backscattered signals, polarimetric SAR (PolSAR) data are richer in information content, as they capture changes in both intensity and phase of the electromagnetic waves and are expected to have a greater contribution in remote crop-type identification applications [32]. As the scientific field of Radar Polarimetry progresses, many polarimetric decomposition techniques have been proposed for quantitatively analyzing PolSAR data and extracting information about the scattering characteristics of Earth's objects [33], and many of them have been successfully employed in crop classification studies [34]. $H/A/\bar{\alpha}$ decomposition method, conceptualized by Cloude and Pottier (1997) [35], is one of the most popular among them [36] and it is based on the eigendecomposition of the multilooked polarimetric coherency or covariance matrix. This method was initially developed for the analysis of quad-pol data and it was later adapted for the dual-pol data case [37]. Covariance matrix's eigenvectors is considered to represent the scattering mechanisms, while the associated eigenvalues express the contribution of each mechanism to the total scattered power [38]. By applying this technique, three main polarimetric parameters can be extracted: entropy (H), anisotropy (A), and mean alpha angle ($\bar{\alpha}$). Entropy indicates the degree of statistical disorder of the scattering process, anisotropy is a measure of the relative importance of the secondary scattering mechanisms, providing valuable information in cases of targets with high values of entropy (H > 0.7), and mean alpha angle value represents the dominant mechanism taking place in the scattering phenomenon, being single-bounce scattering, volume scattering, or double-bounce scattering for values close to 0°, 45°, and 90°, respectively [39]. Apart from the three above decomposition parameters, several others polarimetric parameters can be obtained by the specific method, using the open source "Polarimetric SAR data Processing and Education Toolbox" (PolSARpro) [40], provided by the European Space Agency (ESA). Some of them contain information about the eigenvectors and eigenvalues of the covariance matrix, while others are calculated based on different combination of H and A or they are related to Shannon entropy, a parameter that also quantifies the degree of randomness in the scattering phenomenon [41].

The potential of Sentinel-1 PolSAR data has been moderately examined in several application contexts, such as land-cover mapping [42–47], crop monitoring [11,28,48–53], crop yield estimation [54], crop damage detection [55], as well as in other specialized research areas, such as surface soil moisture estimation [56] and flood extent mapping [57]. Even though numerous studies have examined and demonstrated the contribution of PolSAR data collected from various SAR missions, such as Radarsat-2, in effective crop mapping [58–60], there is only a handful of relevant applications that utilize Sentinel-1 PolSAR data [32,42,61–67]. This limited interest might be justified, considering that the pre-processing workflow of Sentinel-1 PolSAR data is a non-trivial and computationally expensive task. These studies undertaken to explore the usefulness of Sentinel-1 PolSAR data exhibit high heterogeneity concerning the study area characteristics, as well as, the input datasets and classification algorithms that were employed. Some of these studies use only polarimetric input features to build their crop classification models, reporting satisfactory overall accuracies from up to 96% [32], while some of them incorporate polarimetric features as supplementary information in combination with Sentinel-1 backscattering data [64,65,67], reporting contradictory results about the added value of PolSAR data. In most cases, H, A, $\bar{\alpha}$ parameters derived from Cloude–Pottier polarimetric decomposition were used, as well as the elements of the covariance matrix. Additionally, two of these studies performed feature importance estimation analysis [32,63], demonstrating that Sentinel-1 polarimetric attributes are more valuable compared with its corresponding backscattering data and highlighting that parameters related with Shannon entropy contain valuable information content for effectively discriminating crop types.

The synergistic use of optical and SAR satellite data is an increasingly adopted strategy in crop classification studies [3]. By using multi-sensor information, supplementary and

temporally dense information about vegetation's properties can be collected [2,68], allowing to capture significant crop-specific phenological changes within crops' growth cycles [34,69]. According to the findings of numerous studies [20,21,70–74], integrating data from both Sentinel-1 and Sentinel-2 missions is of great value to discriminate different crop types, since better classification results are obtained than employing optical or SAR data alone. The rich potential of this approach is clearly demonstrated by the research of van Tricht et al. (2018) [14] that examined multiple object-based classification scenarios, using as input data different combinations of Sentinel-1 VV and VH polarized backscattering values and Sentinel-2 images, and found that, in all cases, the joint use of both types of data resulted in higher overall accuracy. At this point, it should be noted that most of the above studies make use only of the amplitude information of the collected SAR backscattering signals, while ignoring the phase information contained in Sentinel-1 PolSAR data. Despite the fact that there are many recent publications suggesting the integration of these two types of satellite data in crop classification tasks [32,75], research in this direction remains scarce. To the best of our knowledge, there is only one study focusing on evaluating both Sentinel-1 polarimetric data and Sentinel-2 optical data contribution in differentiating different types of crops [62], reporting some very promising results for accurately mapping crops. These findings are in agreement with another crop classification study carried out by Gao et al. (2018) [16], who demonstrated that the integration of single date Gaofen-3 PolSAR an Sentinel-2A optical data resulted in an improved overall accuracy compared with the classification models built on optical or PolSAR data alone.

The increasing scientific interest in utilizing various types of remotely sensed data combined with the continuous advancement in remote sensing systems has lead to the accumulation of dense multi-temporal imagery with richer information content and finer spatial resolution [76] and, as a result, to the formation of very large datasets with numerous features [77]. Regarding the task of remote identification of crops, such high dimensional datasets, not only demand for high computational resources, but also may contain redundant, irrelevant, or misleading information that could diminish significantly the performance of Machine Learning (ML) classifiers [78]. These negative aspects could be compensated by applying feature selection methods in order to extract an optimal subset of predictors [2]. Indeed, various feature selection and feature importance estimation strategies, especially Random Forest based importance estimation, have been implemented by a considerable number of crop classification studies [68,79–83]. Another high quality and extensively used feature selection strategy is Genetic Algorithms (GA). This particular method exhibits numerous advantages, such as its wide applicability and effectiveness in dealing with complex problems [84,85], rendering it a very attractive option for feature selection tasks. Despite the great popularity of GAs in numerous scientific fields [86], this technique has been moderately used in land-use/land-cover classification studies for feature selection [77,87–91] and in optimizing the parameters of the employed classification algorithms [76,91–94].

The research objectives of this study are to explore the capability of PolSAR data to classify different crop types under diverse experimental setups, (i) as independent input and (ii) as complementary information combined both with cloud-free and with clouded Sentinel-2 imagery. Moreover, we aim to assess the importance of the different input time-series features in order to design a crop classification pipeline that is both accurate and efficient. To this end, an object-level crop classification approach was adopted in order to generate crop maps of an agricultural region in Navarre, Spain. Specifically, several classification scenarios were examined, leveraging multi-temporal PolSAR and optical data from the Sentinel-1 and Sentinel-2 missions and a Support Vector Machines (SVM) classifier. Cloude–Pottier polarimetric decomposition was employed in order to extract polarimetric attributes from Sentinel-1 time-series data. Several studies have used some of the $H/A/\bar{\alpha}$ polarimetric parameters in crop classification tasks. However, in this work we assess for the first time the usefulness of the complete set of 23 $H/A/\bar{\alpha}$ decomposition polarimetric parameters, as provided by the PolSARpro software. In total, multi-temporal optical and

polarimetric features formed a large feature space of 818 attributes. In an attempt to derive an optimal feature subset of this big feature space, we also implemented a GA as a feature selection technique. Apart from this, we also performed the computational demanding analysis of carrying out 100 independent GA experiments and recording the selection frequency of each individual feature as a means to identify the most informative attributes for the multi-class crop classification task at hand. In summary, the main contributions of this work are the following:

1. The extraction of the complete set of $H/A/\bar{\alpha}$ polarimetric indicators from the Sentinel-1 time-series data and the assessment of their capability of classifying different crop classes using SVM, which yields promising results with an overall accuracy of more than 82%.
2. The demonstration of the added value that PolSAR Sentinel-1 data offer when combined with Sentinel-2 optical data for crop classification, in areas that suffer from extended cloud coverage.
3. The implementation of a custom but robust GA as a feature selection method, which provides the optimal feature sets for crop classification.
4. A statistical analysis of GA's feature selection results as a means to estimate features' relative importance and suggest optimal feature sets of reduced dimensionality (more than 85% decrease). We show that the spectral and polarimetric characteristics of these optimal features, in different temporal milestones, can be explained by the phenology evolution of the different crops included in the dataset.

2. Materials

2.1. Study Area

The study area extends across a small agricultural area of the Navarre district, located in the northeastern part of Spain (Figure 1). The area of interest surrounds the city of Pamblona, the capital of Navarre, and occupies approximately 215 km² that comprises 12,329 crop fields. Navarre's province is covered by irrigated valleys and forested mountains, with its northern part being dominated by the Pyrenees mountain range. The agricultural zone of interest is characterised by significant fragmentation, resulting in lower yields compared to the rest of the country [95]. At the same time, the rates of artificial fertilizers' use in the region exceeds the national average rate [95]. The 10 most dominant crop types of the area were taken into account: soft wheat, barley, oats, rapeseed, shrub grass, sunflower, maize, broad beans, vineyards, and cherry trees. The average area of a field was approximately 2 ha.

2.2. Reference Data

The Land Parcel Identification System (LPIS) contains the field polygons and the farmer-declared crop type for each polygon [19]. In this work, we use the regional LPIS data of 2018. LPIS was offered by INTIA, a public company that is part of Spain's Department of Rural Development, Environment, and Local Administration, being, also, the paying agency for the Navarre district, and responsible for all CAP compliance inspections in the area. Figure 2 illustrates the onset and duration of the principal growth stages for the major crops of the study area, along with the corresponding Sentinel-1 and Sentinel-2 acquisitions. The LPIS polygons were used for generating a field-based feature space, as well as for training the SVM classifier and evaluating the quality of the generated classification models using the crop type declarations.
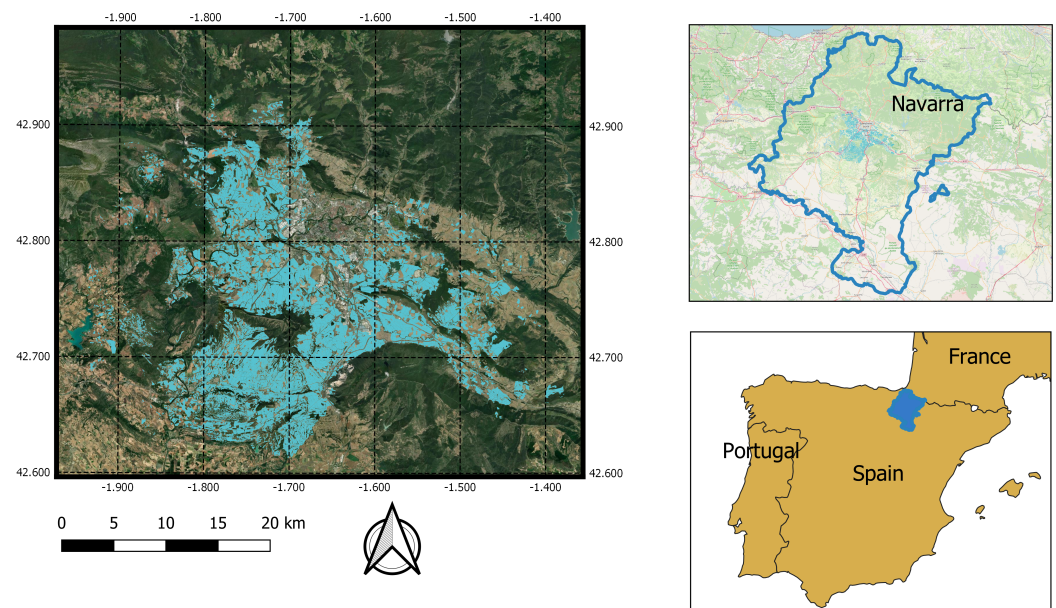
Figure 1. Study area located in Navarre, Spain. The scale is referred to the map on the left where the fields of interest are illustrated in light blue color. On the upper right map, the dark blue line indicates the borders of the entire province of Navarra. In the lower right map, we highlight the location of Navarra with respect to the entire country.
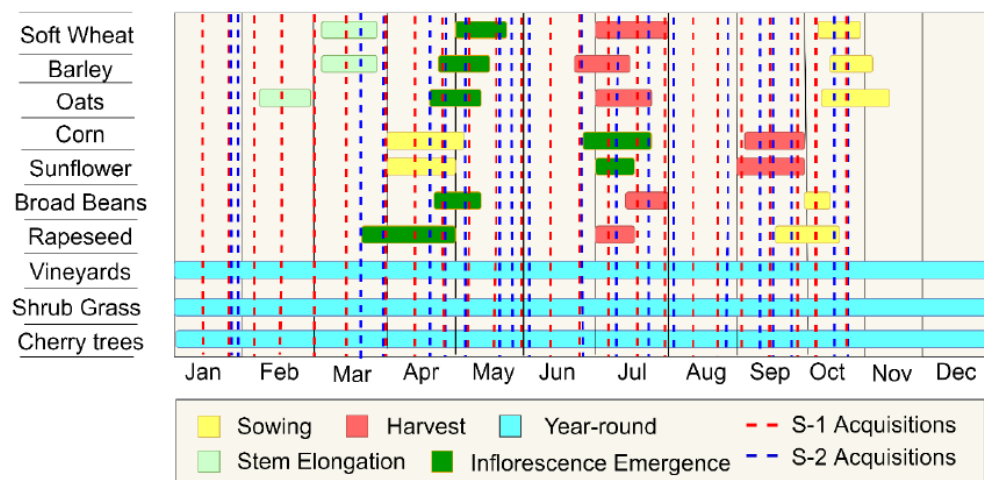
Figure 2. A timeline of the growth stages of the major crops in the study area, reworked from [96], presented with Sentinel-1 (red color) and Sentinel-2 (blue color) acquisition dates.

2.3. Satellite Data

2.3.1. Sentinel-1 Data

The Sentinel-1 satellites are equipped with a dual-polarized (VV, VH) C-band SAR sensor, operating at 5.045 GHz [97]. The sensor's incidence angle ranges between 29.1° and 46.0° [11] and data can be collected in both ascending and descending orbit pass directions. The Sentinel-1 mission operates in four different acquisition modes (Stripmap, Interferometric Wide swath (IW), Extra-Wide swath, Wave) [12] and has a high revisit time of 6–12 days (now 12 days due to the loss of Sentinel-1B). In this work, we used 24 Sentinel-1A and Sentinel-1B acquisitions from mid-January to late October of the 2018 growing season. The images were downloaded as Level-1 SLC products and were acquired in IW swath mode at ascending orbit direction. Each Sentinel-1 IW SLC product captures approximately a swath of 250 km in length, at 5 m × 20 m spatial resolution in the azimuth and range direction, respectively. Additionally, it comprises 3 sub-swaths per polarization and each sub-swath is divided into 9 bursts.

2.3.2. Polarimetric Data Representation

Fully polarimetric SAR data, captured in different polarization channels (HH, HV, VV, VH), are often combined into a 2 × 2 complex scattering matrix for each image cell/pixel (Equation (1)), which is considered an adequate descriptor of point/pure single scatterers [59].

$$[S] = \begin{bmatrix} S_{HH} & S_{HV} \\ \S_{VH} & S_{VV} \end{bmatrix} \tag{1}$$

The scattering matrix for dual-polarized SAR systems (e.g., Sentinel-1) has lower dimensionality and contains half of the polarimetric information involved in quad-polarised data [98]. Specifically, for the Sentinel-1 case, backscatter measurements collected in VV and VH polarization channels, is often incorporated into a scattering vector $\vec{k} = [S_{VV}, S_{VH}]^T$. By spatially averaging this scattering vector, 2 × 2 multi-looked covariance matrix C_2 is generated at pixel level, as expressed in Equation (2):

$$\langle C_2 \rangle = \langle \vec{k} \cdot \vec{k}^{*T} \rangle = \begin{bmatrix} C_{11} & C_{12} \\ C_{21} & C_{22} \end{bmatrix} = \begin{bmatrix} \langle | S_{VV} |^2 \rangle & \langle S_{VV} S_{VH}^* \rangle \\ \langle S_{VH} S_{VV}^* \rangle & \langle | S_{VH} |^2 \rangle \end{bmatrix} \tag{2}$$

where $\langle ... \rangle$ denotes multi-looking processing, * complex conjugation, and T transposition. The diagonal elements of the covariance matrix (C_{11}, C_{22}) represent the backscattering coefficients in VV, VH polarization channels [11], respectively, while C_{12}, C_{21} elements express the complex correlation of back-scattered information between VV, VH polarization channels [67]. Deriving the covariance matrix from the vectorized scattering matrix is essential for the accurate characterization of distributed targets, such as vegetation [99].

For the purposes of this study, multi-temporal data for 23 polarimetric parameters (Table 1) were derived from the dual-pol Sentinel-1 PolSAR data by employing the H/A/$\overline{\alpha}$ polarimetric decomposition technique in order to obtain information about the scattering mechanisms of each crop type. By applying this method, covariance matrix data of each SAR image was subjected to an eigen-decomposition process. Each one of the two eigenvectors derived from a 2 × 2 covariance matrix is related to one of the two scattering mechanisms occurring at the particular image cell, while the corresponding eigenvalues quantify the relative importance of each scattering mechanism to the total measured backscattered signal [33].

Specifically, through the process of eigen-decomposition, covariance matrix is expressed as a weighted sum of two matrices, $[C_2]_1$ and $[C_2]_2$, representing the two different scattering mechanisms occurring at pixel level:

$$\langle [C_2] \rangle = [U] \begin{bmatrix} \lambda_1 & 0 \\ 0 & \lambda_2 \end{bmatrix} [U]^{T*} = \sum_{i=1}^{2} \lambda_i \vec{u_i} \vec{u_i}^{T*} = \lambda_1 \vec{u_1} \vec{u_1}^{T*} + \lambda_2 \vec{u_2} \vec{u_2}^{T*} = \lambda_1 [C_2]_1 + \lambda_2 [C_2]_2 \tag{3}$$

$$[U] = \begin{bmatrix} U_{11} & U_{12} \\ U_{21} & U_{22} \end{bmatrix} = [\vec{u_1} \vec{u_2}] \tag{4}$$

where $[U]$ is the orthogonal unitary matrix, $\vec{u_i}$ (i = 1, 2) is the eigenvector i and λ_i (i = 1, 2) is the corresponding eigenvalue i.

Additionally, each C_2 eigenvector $\vec{u_i}$ can be parameterized, using two angular variables, α_i and δ_i, denoting the scattering mechanism and the phase angle, respectively [61] (Equation (5)).

$$\vec{u_i} = [\cos a_i, \sin a_i e^{j\delta_i}]^T, \quad i = 1, 2 \tag{5}$$

Using the calculated eigenvectors and eigenvalue we are able to compute polarimetric parameters. The main polarimetric parameters derived by Cloude–Pottier decomposition are Entropy H, Anisotropy A and mean alpha angle $\overline{\alpha}$ and they are determined by the following equations:

$$H = \sum_{i=1}^{2} p_i \log_2 p_i \tag{6}$$

$$A = \frac{\lambda_1 - \lambda_2}{\lambda_1 + \lambda_2} \tag{7}$$

$$\bar{\alpha} = \sum_{i=1}^{2} p_i \alpha_i = p_1 \alpha_1 + p_2 \alpha_2 \tag{8}$$

where pseudo-probabilities p_i represent the relative importance of C_2 eigenvalues λ_i (Equation (9)), allowing for a probabilistic interpretation of the scattering phenomenon.

$$p_i = \frac{\lambda_i}{\sum_{i=1}^{2} \lambda_i}, \quad i = 1, 2 \tag{9}$$

According to this view, mean delta angle $\bar{\delta}$ is mathematically expressed in a similar way to mean alpha angle $\bar{\alpha}$, as expressed in Equation (10). Furthermore, Shannon Entropy (SE) can be obtained by the covariance matrix (Equation (11)), expressing the degree of randomness of the scattering process.

$$\bar{\delta} = \sum_{i=1}^{2} p_i \delta_i \tag{10}$$

$$SE = \log\left(\pi^2 e^2 \mid C^2 \mid\right) = SE_I + SE_P \tag{11}$$

This polarimetric parameter can also be expressed as a sum of two measures SE_i and SE_p, quantifying the degree of randomness related with changes in the back-scattered signal intensity or phase, respectively [63] (Equations (12) and (13)).

$$SE_i = 2\log\left(\frac{\pi e \, Tr[C_2]}{2}\right) \tag{12}$$

$$SE_p = \log\left(4\frac{det[C_2]}{Tr[C_2]^2}\right) \tag{13}$$

where *Tr* and det represent the trace and determinant of the matrix, respectively.

Table 1. Summary of H/A/$\bar{\alpha}$ polarimetric parameters.

Parameter Name	Parameter Notation
mean scattering alpha angle	alpha
first scattering alpha angle	alpha1
second scattering alpha angle	alpha2
Anisotropy	*anisotropy*
H-A combination 1 $[H \cdot A]$	combination_HA
H-A combination 2 $[H \cdot (1 - A)]$	combination_H1mA
H-A combination 3 $[(1 - H) \cdot A]$	combination_1mHA
H-A combination 4 $[(1 - H) \cdot (1 - A)]$	combination_1mH1mA
mean scattering delta angle	delta
first scattering delta angle	delta1
second scattering delta angle	delta2
entropy	entropy
Shannon entropy	entropy_shannon
Shannon entropy intensity	entropy_shannon_I
Shannon entropy intensity normalized	entropy_shannon_I_norm
Shannon entropy polarization	entropy_shannon_P
Shannon entropy polarization normalized	entropy_shannon_P_norm
first eigenvalue	l1
second eigenvalue	l2
mean eigenvalue	lambda
probability 1	p1
probability 2	p2

Sentinel-1 multi-temporal images underwent a series of pre-processing steps, in order to obtain time-series data for each one of the 23 polarimetric parameters. In more detail, we followed the pre-processing workflow recommended by Mandal et al. (2019) [100], using ESA's Sentinel Application Platform (SNAP) v.7.0.0 and PolSARpro v.6.0 tools [101], which is schematically presented in Figure 3. The first step of this pre-processing chain was the splitting step. As our study site was situated within two successive sub-swaths of the Sentinel-1 images, these sub-swaths were separated and processed individually, using Sentinel-1 TOPS Split operator. Splitting operation was followed by performing orbit correction at each sub-swath, using an Apply-Orbit operator. This pre-processing step allows for accurate image geocoding, making use of the precise orbit files contained in each product's metadata. After applying orbit files, each sub-swath was radiometrically calibrated and saved in complex-valued format, required for the computation of C_2 matrix. SAR calibration allows for directly relating image's pixel values to the backscattering signals of the scene [102]. Next, Sentinel-1 Back Geocoding operator was applied to each sub-swath (slave) in order to co-register it to the corresponding sub-swath of the master image (captured on 12 January 2018), using the SRTM 3Sec HGT Digital Elevation Model (DEM), and create a stack of multi-temporal data [100]. Afterwards, TOPSAR Deburst module was used for joining separate successive bursts of each sub-swath into a single product. After debursting, separately processed sub-swaths were merged, creating a larger sub-scene. The following step was to reduce the original image size to the study area's extend in order to decrease processing time, using the "Subset" module. Subsequently, after deleting metadata baseline information from the image stack, Stack Split operator was used, to separate single date products under processing from the master image, and scattering matrix elements were exported from SNAP to the PolSARPro format. Each SAR image was then imported into the PolSARpro software and was multilooked (spatially averaged) with a window size of 4×1 (in range and azimuth direction, respectively) pixels to create ground ranged squared pixels. After generating the multi-looked C_2 matrix for each pixel, each SAR image was filtered by using a Refined Lee Filter [103] with a window size of 7×7 pixels, in order to mitigate speckle noise. The last step of the pre-processing chain was the application of the "Range Doppler Terrain Correction" algorithm, by using a SRTM (Shuttle Radar Topography Mission) 1 arc-second Digital Elevation Model (DEM) and by employing a bilinear interpolation resampling method. As a result, SAR images' geometric distortions, due to sensor's varying viewing angle and topological variations, were corrected and a better geometric representation of Earth's surface was obtained [104].

2.3.3. Sentinel-2 Data

Sentinel-2 satellites collect multi-spectral optical imagery of high spatial resolution every 5 days [105]. Both satellites carry a Multi-Spectral Imaging Instrument (MSI) with a swath width of 290 km, which is designed to capture electromagnetic waves of the visible and near infrared region to the shortwave infrared region of the spectrum. More specifically, Sentinel-2 MSI captures targets' reflectance responses in 13 bands of different wavelengths, namely B01, B02, B03, B04, B05, B06, B07, B08, B8A, B09, B10, B11, and B12, with various spatial resolutions of 10, 20, and 60 m.

For the purposes of this study, 19 Sentinel-2 Level-1C images, having the minimum cloud coverage over the study area, were retrieved from the Copernicus Open Access Hub during the period January–October 2018, resulting in a dense time-series. The selected acquisition dates are extended across the entire growth cycle of the cultivated crops and is expected to hold important information at key phenological stages, such as flowering, ripening, and harvesting phases. Additionally, the 60 m bands (i.e., B01, B09, and B10) were excluded. Regarding the images pre-processing, Sentinel-2 products were atmospherically corrected to bottom of atmosphere reluctance by using Sen2Cor algorithm in the SNAP software, and all the bands were resampled to 10 m spatial resolution.
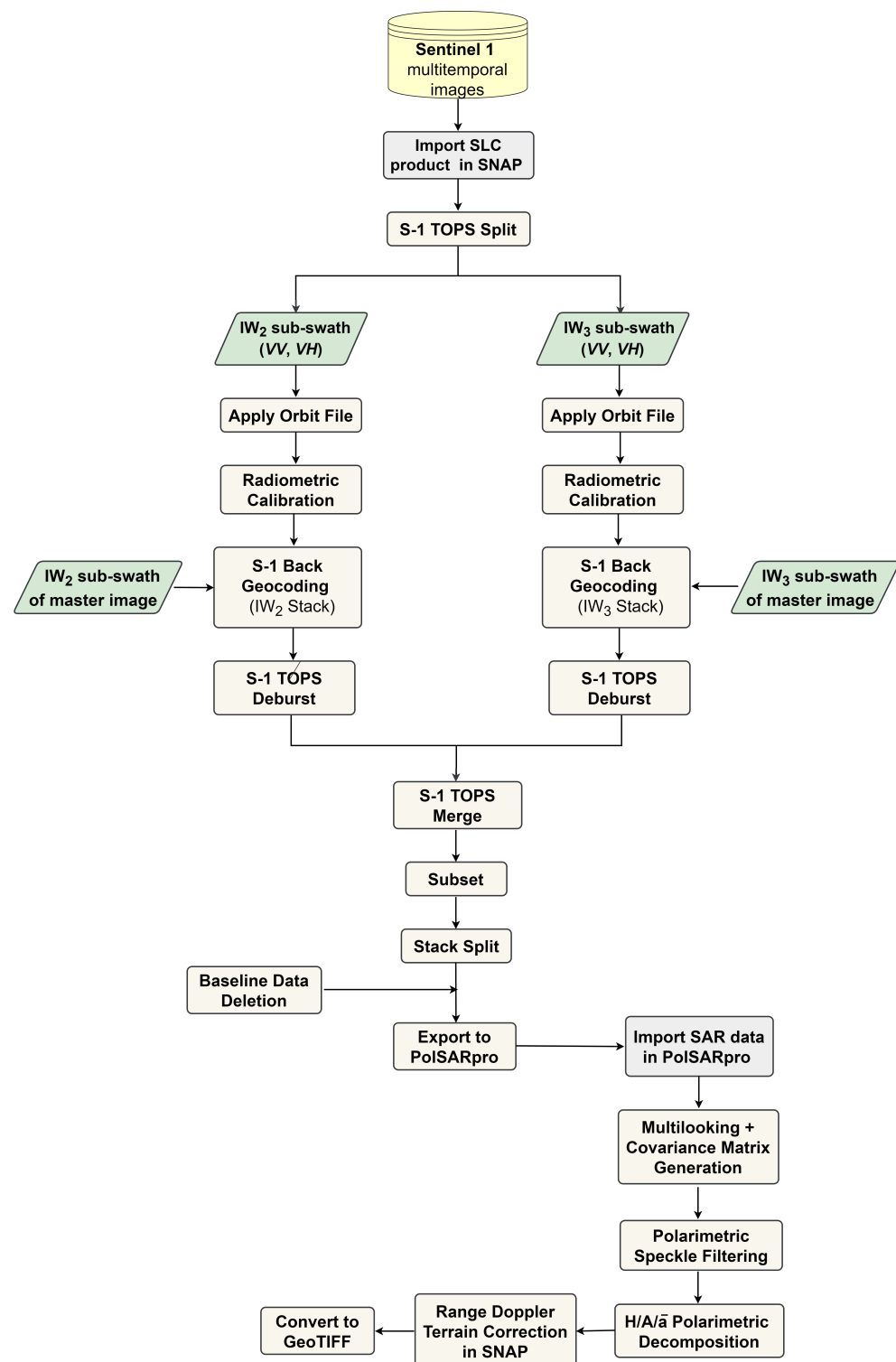
Figure 3. Flowchart of Sentinel-1 data pre-processing.

Apart from using the original Sentinel-2 bands, we evaluated the potential of four vegetation indices, namely the Normalized Difference Vegetation index (NDVI), the Normalized Difference Water Index (NDWI), the Plant Senescence Reflectance Index (PSRI), and the Soil Adjusted Vegetation Index (SAVI), in categorizing the different types of crops of the agricultural study area (Equations (14)–(17)). Vegetation indices are calculated via simple mathematical formulas, by using information of targets' spectral responses at different wavelength intervals [106] and provide valuable, additional information about vegetation's

status and growth, resulting in better separability between different crop classes [107], as demonstrated by numerous crop classification studies [108]. In particular, NDVI [109] is considered the most popular vegetation index in crop monitoring and classification studies [110], being indicative of vegetation's status and photosynthetic activity [111]. NDWI proposed by Gao (1996) [112], is an effective indicator of vegetation's water content [113]. PSRI, defined by Merzlyak (1999) [114] exhibits great sensitivity in the aging stage of plant development. SAVI introduced by Huete (1988) [115] reduces soil effect in NDVI values [106] and is descriptive of crop's structural characteristics, such as leaf area index [116].

$$NDVI = \frac{\rho_{NIR} - \rho_R}{\rho_{NIR} + \rho_R} = \frac{B4 - B8}{B4 + B8} \tag{14}$$

$$NDWI = \frac{\rho_G - \rho_{NIR}}{\rho_G + \rho_{NIR}} = \frac{B3 - B8}{B3 + B8} \tag{15}$$

$$PSRI = \frac{\rho_R - \rho_G}{\rho_{NIR}} = \frac{B4 - B2}{B6} \tag{16}$$

$$SAVI = \frac{\rho_{NIR} - \rho_R}{\rho_{NIR} + \rho_R + L} * (L + 1) \tag{17}$$

3. Methods

The method of this work is schematically presented in Figure 4. The rest of this section elaborates on the individual steps.
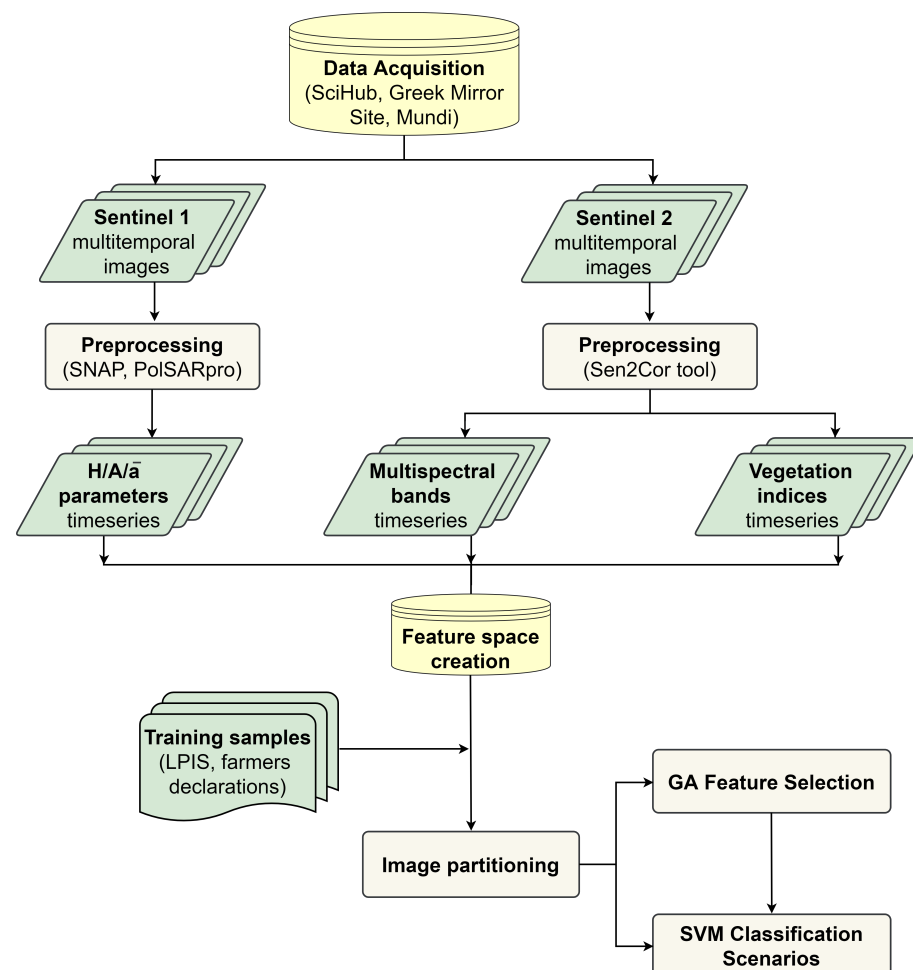

Figure 4. The methodological workflow of this study.

3.1. Image Partitioning and Feature Space Creation

In this study, an object-based image analysis approach was followed, taking into account the fact that is more advantageous compared to pixel-based approaches in crop classification tasks that deal with fields of considerable size [3,26,117]. Specifically, each image was segmented into field entities based on the LPIS' polygons. This procedure resulted in the formation of 12,329 reference fields. Subsequently, the reflectance value of each field was calculated, for all features, as the mean value of the pixels contained in it. The code number, the number of fields, as well as the approximate value of the total area covered in hectares corresponding to each crop class are presented in Table 2.

Table 2. Main characteristics of each crop type.

Crop Type	Class Code	Number of Fields	Total Area (ha)
soft wheat	1	5461	10,922
barley	5	3609	7218
oats	8	1172	2344
rapeseed	35	708	1416
shrub grass	65	326	652
sunflower	33	285	570
maize	4	223	446
broad beans	41	210	420
vineyards	102	208	416
cherry trees	110	127	254

The feature space of this study (Table S1) is made up of 818 features extracted from the multi-temporal Sentinel-1 and Sentinel-2 images. More specifically, feature space comprises the Sentinel-2 multi-spectral bands (190 variables), and vegetation indices (76 variables), as well as a total number of 552 polarimetric variables derived from Sentinel-1 time-series.

3.2. Genetic Algorithm

In our research, we implemented a custom GA in order to derive the most informative optical and polarimetric features for the crop classification problem at hand. A GA is an evolutionary, metaheuristic optimization method, conceived by Holland (1992) [118], and inspired by Darwin's theory of biological evolution [119]. GAs are part of the family of population-based algorithms [120]. Based on the theoretical background of this method, problem features are called genes, which are initially organised in a random way into different subsets of the total feature space, named chromosomes [121]. These feature subsets represent candidate solutions for the optimization problem at hand [122]. A GA is practically an iterative process of evaluating chromosomes' quality using a fitness function and of improving chromosomes' fitness through selection, crossover, and mutation processes, by which eventually an optimal feature subset is derived [86,123].

GA implementation requires the definition of a large set of hyperparameters by the user, which significantly affect its effectiveness [123]. Population size, as well as crossover and mutation probabilities, are considered GA as the most important parameters and selecting them properly, taking into account the nature of the specific optimization problem at hand [124], is crucial for GA performance [119]. In our research, population size was set to 100 chromosomes, being a common choice in the literature [125] and ensuring satisfactory exploratory ability of the solution space with a reasonable computational cost [126]. Crossover probability was set to 0.9, considered an appropriate value for allowing the proper exploitation of the current population's genetic material and the formation of better chromosomes [84]. Concerning the mutation process, we defined two mutation probabilities, one related to the probability of a chromosome being subjected to mutation and another related to the probability of a particular gene being mutated, following Wirsanky's methodology [84]. The first one was set to the relatively low value of 0.2 for improving population diversity, while preventing the GA to turn into a random

search method [86,121]. The second one was calculated by the ratio $\frac{1}{N}$, where N symbolises the chromosome length [84].

Regarding the design of chromosomes, each gene was coded as a string, referring to one of the 818 multi-temporal features of the study. Each one of the first-generation chromosomes, representing a feature subset, was randomly initialised with a number of unique genes. In our attempt to determine an optimal chromosome length (number of genes), we examined how this parameter affects the highest weighted average f1 score obtained at GA's convergence, as well as the mean computational time required for each iteration. In further detail, 12 GA implementations were performed, testing multiple values of the chromosome length parameter, ranging from 10 to 120 with a step size of 10 genes. The results of these experiments are presented schematically in Figure 5.
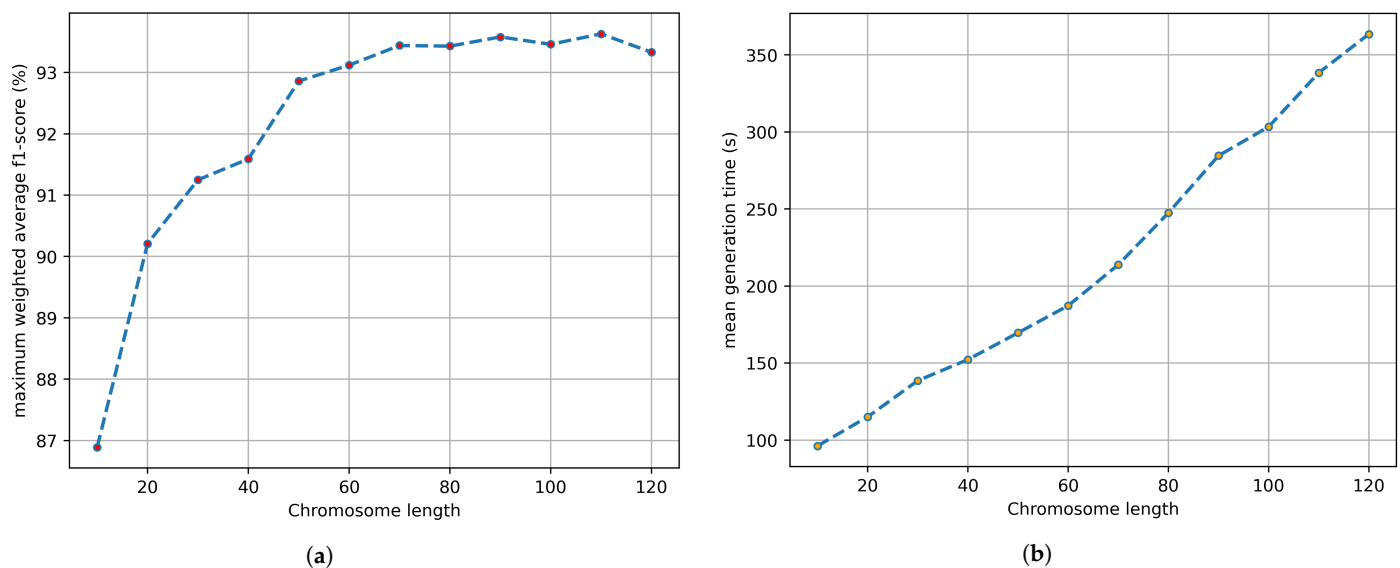
Figure 5. (**a**) The maximum weighted f1 score obtained for different values of chromosome length. (**b**) The mean generation time required for different values of chromosome length.

According to Figure 5a, as the chromosome length increases from 10 to 70 genes, the maximum weighted average f1 score achieved by the GA at convergence sharply and gradually improves by 6.5%. However, implementing the GA with a chromosome length of more than 70 genes, does not contribute to a significant further improvement of GA's performance, as the maximum weighted average f1 score obtained reaches a plateau of approximately 93.5%. This might be explained by the fact that the full feature space contains plenty of redundant features and, consequently, implementing GA with very large chromosomes does not lead to better outcomes. Based on Figure 5b, the relationship between chromosome length and the mean generation time appears to be proportional. This experimental result is quite reasonable, considering that the greater the number of genes (features) contained in a chromosome, the more computational time is needed for training the SVM classifier for each one of population's chromosomes. Aiming to extract an optimal subset of spectral-temporal features with rich information content for accurately discriminating the crop types of the studied agricultural region, we considered the value of 80 genes as an optimal one for the implementation of GA, close to the minimum threshold (70 genes), in order to achieve the highest possible classification accuracy with the lowest possible computational cost.

A second-degree polynomial SVM was employed as the function for assessing the ability of each chromosome to effectively discriminate the crop types of the study area at each iteration. SVM is a non-parametric supervised machine learning algorithm [127]. This model depends on three important hyperparameters, namely the cost parameter $\mathcal{C}$, kernel bandwidth γ, and the independent term of the kernel function, denoted by *coef0*. The cost parameter determines the acceptable number of misclassification errors and sig-

nificantly affects model's generalization ability [128]. In other words, the higher the cost parameter value, the higher the penalties imposed for margin violations [129], resulting in the formation of complex decision boundaries and overfitting [107,130]. The complexity of the decision boundary also depends on the γ parameter, which determines the influence range of its training sample [131]. The kernel's independent term *coef0* determines the degree of influence of the high-degree polynomials versus low-degree polynomials in the classification model [131]. In our implementation, SVM was parameterized as follows: cost parameter = 1, independent coefficient = 1, and gamma parameter = 0.01. This parametrization was based on preliminary experiments in order to combine high performance with low computational complexity. Weighted-averaged f1 score, a classification accuracy metric, was used as the fitness value of the chromosomes, which is calculated based on the support of each class [132]. Next, a probabilistic selection strategy was employed, i.e., the roulette wheel or fitness proportional selection method [86], for choosing the fittest parent chromosomes to take part in the crossover process. In more detail, according to this method, the probability $p(i)$ of a chromosome i to be selected is proportionate to its fitness value $f(i)$ and is calculated using the formula $p(i) = \frac{f(i)}{\sum_{i=1}^{n} f(i)}$ (n is the population size). Apart from selecting parent chromosomes with the roulette wheel method, an elitism strategy was applied, conveying the Darwinian principle of "survival of the fittest" [91]. By adopting this strategy, the fittest chromosomes of each generation are retained and included in the set of parent chromosomes. More specifically the percentage of the elite parents was set to 20% of the total number of parent chromosomes.

After the selection process, single point crossover was employed [120]. According to this method, each pair of successive parent chromosomes participates in a probabilistic crossover process with a probability of 0.9. If crossover occurs, a particular point is randomly selected, where parent chromosomes are split into two parts, and exchange their genetic material for creating a pair of two new chromosomes. Otherwise, if crossover does not occur, parent chromosomes directly pass to the next generation of chromosomes. Subsequently, every chromosome of the new generation is mutated with a probability of 0.1. If chromosome mutation occurs, every gene is mutated with a probability $\frac{1}{N} = 0.01$, which means that is replaced with another randomly selected feature from the entire feature space; otherwise, chromosome remains immutable. Finally, GA terminates when 100 iterations are completed or when the population's maximum weighted f1 score does not improve for 5 successive iterations. After its termination, GA returns the optimal feature subset, represented by the best chromosome of the final generation. Our custom GA was implemented in Python. GA procedure steps, as well as their parametrization details, can be found in the Supplementary Materials in Figure S1 and Table S2, respectively.

3.3. Crop Classification

Every crop classification procedure of this study was performed using the SVM classification algorithm. This particular method was selected, considering its high effectiveness, robustness, and generalization ability, especially when dealing with high dimensional, low quality, imbalanced, or scarce data [133,134]. Apart from this, SVM algorithm has already been widely used and proved effective in crop type mapping applications using remotely-sensed data [19,130,134]. Specifically, four SVM classification models were produced, based on different sets of input data. In more detail, SVM classifier was trained using as input data: (1) Sentinel-2 optical features (S2 model), (2) Sentinel-1 polarimetric features (S1 model), (3) Sentinel-1 polarimetric features and Sentinel-2 optical features combined (S1/S2 model), as well as (4) an optimal subset of 80 mixed-type features obtained from a single GA implementation (GA model). Additionally, in an attempt to estimate features' relative importance, we carried out 100 GA runs and recorded how often a particular feature appeared in the 100 optimal feature subsets that were derived. We decided to conduct 100 individual experiments, since this number is relatively large, allowing for a statistical analysis of satisfactory quality with marginally permissible computational costs. The selection frequency of each feature could be interpreted as a measure of its relative importance

for the crop classification problem at hand. Based on GA's feature selection results, we obtained a sorted list of the most important individual features that were exploited as input data for the construction of ten additional crop classification models. For all classification scenarios examined, SVM was implemented by using a second degree polynomial kernel and its hyperparameters were optimized using the grid-search method. The optimal values that were derived for each parameter and for all the investigated classification scenarios are presented in Table S3. Moreover, since we examine a multi-class crop classification problem, "one-against-one" strategy was employed, combining 45 binary SVM classifiers for each pair of classes in order to construct a single multi-class classifier [77]. Reference samples were randomly split into a training (30%) and a testing set (70%), resulting in a total number of 3698 training fields. The performance of each crop classification model was evaluated using four accuracy metrics: overall accuracy (OA), as well as class-specific f1-scores, user's accuracy (UA), and producer's accuracy (PA). The classification results were averaged over 10 runs for each scenario.

4. Results

In this section, we present a comparative analysis for the performance of the SVM algorithm in crop type mapping, using diverse experimental setups. Specifically, in Section 4.1 we have used the actual Sentinel-1 and Sentinel-2 data as derived from the corresponding satellites and we compare the performance of the SVM model using different features as input. Table 3 presents the overall comparison of the different experiments for multiple metrics. The main result of this section is illustrated in the last row of the table and corresponds to the model that utilizes multiple GA runs (more details in Section 4.1.4). Analytic metrics for all crop types of this model can be overviewed in Table 4. Following, in Section 4.2 we have applied artificial cloud masks in the Sentinel-2 time-series to simulate a clouded scenario. Table 5 illustrates the performance of the SVM models trained in the different clouded input feature spaces. In this case, the same model as before (i.e., the GA with multiple runs) yielded the best performance. However, here we observe a much more significant improvement in both individual and overall metrics compared to the Sentinel-2 model.

4.1. Crop Classification Results

In this section, we present the classification results obtained by using the initial dataset, containing Sentinel-1 and cloud-free Sentinel-2 imagery, as described in Section 2.3. Table 3 shortly presents the overall performance of the SVM models trained with different inputs. S1 and S2 refer to the SVM models trained with the time-series data derived from the Sentinel-1 and Sentinel-2 satellites, respectively, whereas S1/S2 describes the SVM model trained with all available features. On the other hand, GA refers to the model trained with a 80-feature set derived from one single GA run. Finally, the last row of the table presents the results obtained by exploiting 100 GA runs, which is explained in detail in Section 4.1.4.

Table 3. Overall accuracy and macro average values of UA, PA, and f1-score of 5 different SVM classification models constructed based on the original dataset. With bold is highlighted the best model for each metric.

Method	UA	PA	f1-Score	OA
S2	91.06	88.95	89.93	92.42
S1	76.10	67.68	71.12	82.83
S1/S2	91.09	87.99	89.41	92.28
GA	91.85	90.04	90.85	93.58
GA$_{15}$	**92.75**	**90.93**	**91.75**	**94.00**

4.1.1. Crop Classification Results Based on Sentinel-2 Imagery (S2 Model)

The OA and weighted average f1-score achieved by this model are both around 92.40%. As is also discussed in [19], all metrics are quite high for most crop types, demonstrating the

high sensitivity of Sentinel-2 measurements to the distinct biophysical properties of crops. In particular, this model exhibited exceptional distinguishing ability of maize, sunflower, and soft wheat, as it is quantitatively expressed by the high f1-scores values obtained (94.99%, 93.97%, and 93.84%, respectively). However, this is not the case for the three all-year crop classes, namely vineyards, shrub grass and cherry trees, being categorized with relatively low f1-scores below 86.00%. The poorer separability of these three crop types might be justified, considering that their spectral signatures, for the majority of optical features, do not contain any specific temporal characteristics that could distinguish them from the other ones. Especially, shrub grass presents by far the worst performance in terms of f1-score values (81.51%). This vegetation type is of a diverse nature, providing various spectral profiles and, hence, misclassifications are expected. Table S4 presents in detail the performance of the SVM model that was built using as input data only the Sentinel-2 multi-temporal features.

4.1.2. Crop Classification Results Based on the Combination of Sentinel-1 and Sentinel-2 Multi-Temporal Imagery (S1/S2 Model)

In this scenario, we use all the available variables, both optical and polarimetric, to train the SVM classifier. The full integration of features did not result in a performance improvement, compared to the S2 model, achieving an OA of around 92.25%. In terms of the class-specific accuracy metrics, the S1/S2 model achieved comparable or better results concerning the discrimination of the majority of crop classes. Specifically, the inclusion of polarimetric features contributed to a considerable improvement of 1.09% and 1.35% in the f1-scores of maize and rapeseed, respectively. However, it exhibited a poorer performance (up to 2.8%) compared to the S2 model for the all-year crop types, as well as for oats. One possible explanation of this under-performance might be the fact that some polarimetric features, which are included into the input feature dataset, might not be adequately descriptive of the complex scattering processes occurring on the vegetation cover of these particular crop types, causing a confusion to the SVM classifier. Another explanation might be the fact the several crop types, such as oats and soft wheat, may have diverse spectral properties, but quite similar dielectric and structural temporal characteristics during several months of the total observation period, with subtle differences that cannot be captured by Sentinel's 1 dual-polarized sensor, requiring the collection of PolSAR data from a system with full polarization capabilities. Table S5 presents the metrics of the SVM model using both types of data, in detail.

4.1.3. Crop Classification Results Based on Sentinel-1 PolSAR Imagery (S1 Model)

In this scenario, we use only the Sentinel-1 PolSAR features to train the SVM classifier. As expected, the model performs worse without the information of the optical sensor, but interestingly OA is quite decent, with a value of 82.83%. This result shows that polarimetric data are informative enough to adequately classify crops. The classification results of the each crop category are presented in Figure 6 (and Table S6). For some crop types in particular, i.e., maize, barley, sunflower, soft wheat, and rapeseed, the performance is very good. However, per-class accuracies for the all-year crop types (i.e., cheery trees, vineyards, and shrub grass), as well as the broad beans, are significantly low. On the one hand, this classification report demonstrates the rich information content of PolSAR data and showcases its great potential in crop mapping. On the other hand, these results reinforce the argument that the dual-polarized PolSAR data might have the ability to only partially describe scattering characteristics, providing models of limited accuracy.
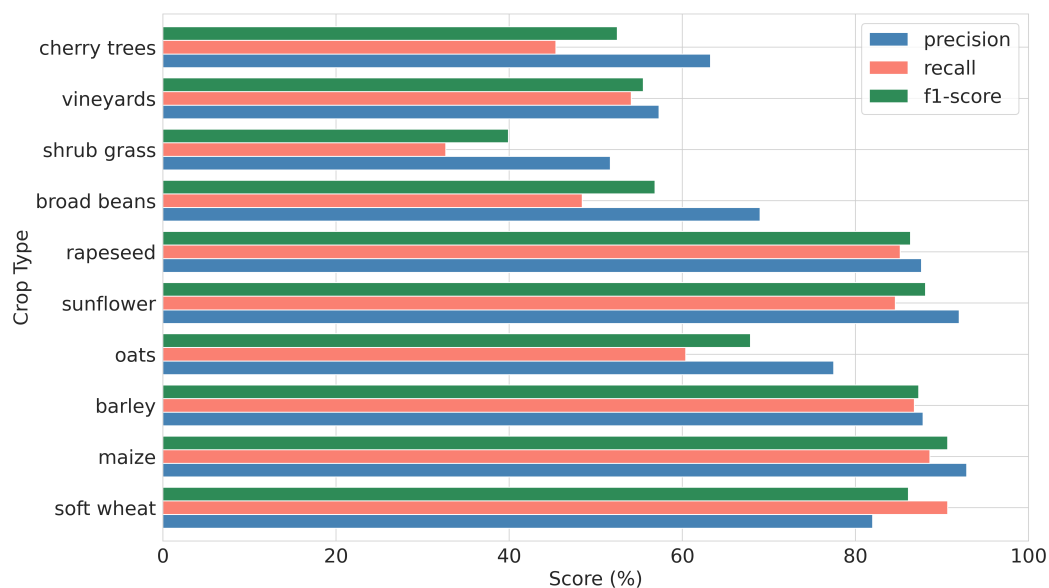
Figure 6. Classification metrics for the different crop type of the S1 model.

4.1.4. Crop Classification Results Based on Genetic Algorithm's Results (GA Model)

The results above indicate that the Sentinel-1 multi-temporal polarimetric features have the ability to distinguish specific crop types. To further investigate the efficient combination of those features with the corresponding Sentinel-2, we used our custom GA to identify the most useful ones. At first, we executed a single run of the GA, which resulted in a list of 80 selected features: 47 optical and 33 polarimetric. This particular model outperforms the previous ones in terms of both OA achieved (93.60%), as well as the weighted average f1-score (93.59%), which is higher by more than 1%. Apart from this, it showcases improvements (1–2%) in most of the individual crop type metrics (Table S7).

Using as input training data the optimal 80-feature subset derived from the GA significantly enhanced the discriminant ability of the SVM classifier. However, one single run might not always result in the best feature subset, considering the inherent probabilistic nature of GAs. In order to overcome this randomness, we carried out a statistical study of the GA, by running 100 separate experiments and, therefore, extracting 100 different optimal feature subsets. In an attempt to identify the most informative features among all 818 features, we counted the number of times t that each feature appeared in these different subsets. This number t can be interpreted as a measure of each feature's relative importance. Figure 7 presents the performance of the SVM model when trained with feature appeared more than t times (GA_t model). Specifically, the red line describes the number of features (right axis) for each different t, whereas the blue and green lines illustrate the OA and the macro averaged f1-score, respectively (left axis). The thresholds that generate optimal solutions, i.e., OA above 93.9% and f1-score above 91.5%, are 13, 14, 15, 16, and 17, which corresponds to 142, 126, 111, 96, and 82 selected features, respectively. This behavior is expected because, as seen in Figure 5, feature sets of more than 80 features can achieve the optimum results, when used to train an SVM model.
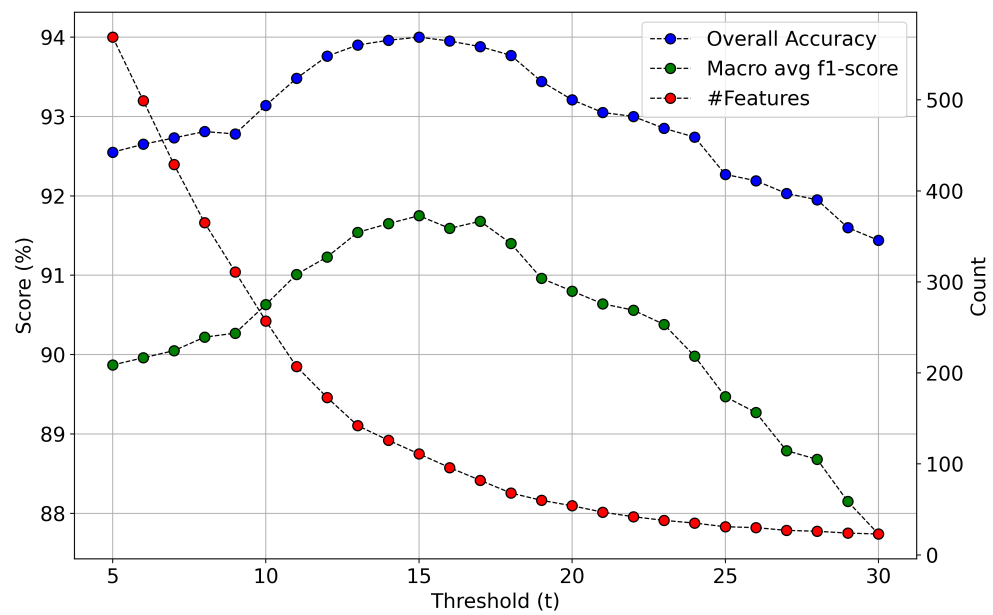
Figure 7. The performance of the SVM algorithm trained with features obtained when we apply the threshold t, in the different 100 subsets results from the GA experiments. The blue and the green lines present the OA and macro averaged f1-score, respectively, and are associated with the left y-axis. The red line indicated the number of features for each different run and is associated with the right y-axis.

Table 4 presents the classification metrics of the GA_{15} model (i.e., the model trained with the set of features derived by using $t = 15$). The scores in each metric and for each crop type are higher compared to the S2 model, up to 3.15%. The macro f1-score has increased significantly from 89.93% to 91.75% that can be translated to an increase of 1.82% average f1-score improvement, in each single crop type, which is a remarkable improvement.

Table 4. Classification report of SVM with 111 features derived when used 15 as threshold.

Crop Type	UA	PA	f1-Score	Support
soft wheat	94.55	95.92	95.23	3823
maize	95.04	96.22	95.60	156
barley	93.84	94.35	94.10	2526
oats	93.70	89.13	91.35	820
sunflower	97.55	92.35	94.86	200
rapeseed	96.17	94.80	95.47	496
broad beans	95.83	90.48	93.06	147
shrub grass	85.67	81.84	83.69	228
vineyards	85.00	91.92	88.27	146
cherry trees	90.17	82.25	85.90	89
macro avg	92.75	90.93	91.75	8631
weighted avg	94.01	94.00	93.98	8631

4.2. Performance of Crop Classification Models in Artificially Generated Cloudy Conditions

In Section 4.1, we highlighted how Sentinel-1 PolSAR features accompanied by the use of a GA, as a feature selection module, can enhance the predictions of a S2 SVM model for crop classification. Although the results indicated a satisfactory improvement, we would not expect any dramatic increase. In our study site, cloud coverage was not a major problem and allowed us to collect temporally dense Sentinel-2 time-series and

generate highly accurate classification models. However, we could expect the PolSAR data to make a real difference in regions where clouds are frequent, such as in Northern European countries. In order to demonstrate this, we generated artificial cloud masks, by applying over our study site the cloud coverage history per month for Copenhagen, Denmark. The coverage ranged from 43% for July to 70% for December.

Specifically, we ingested null values into the Sentinel-2 time-series using the corresponding ratio for each month to simulate the cloud distribution. Then, two SVM models were trained, one using only the new clouded Sentinel-2 data ($S2^c$ model) and another one that combined them with the Sentinel-1 PolSAR ($S1/S2^c$ model). Table 5 presents f1-score, UA, and PA values for the two different models. Unlike the relevant case without artificial clouds, the $S1/S2^c$ model presents a significant increase in almost every single metric, with a notable improvement of more than 3.5% in f1-score.

Table 5. UA, PA, and f1-score of the SVM model when trained (i) only on the artificially-clouded Sentinel-2 time-series ($S2_c$ model), (ii) both on the artificially-clouded Sentinel-2 time-series and the Sentinel-1 PolSAR time-series ($S1/S2_c$ model), and (iii) on the 120 features derived when used 15 as threshold ($GA_{c,15}$).

	f1-Score (%)			PA (%)			UA (%)		
Crop	$S2_c$	$S1/S2_c$	$GA_{c,15}$	$S2_c$	$S1/S2_c$	$GA_{c,15}$	$S2_c$	$S1/S2_c$	$GA_{c,15}$
wheat	88.38	90.91	92.16	91.08	93.65	94.22	85.84	88.34	90.19
maize	90.60	94.02	93.88	89.23	93.40	92.88	92.16	94.72	94.93
barley	85.83	90.51	91.51	85.08	90.04	91.02	86.60	90.99	92.01
oats	76.57	81.30	84.70	71.98	75.09	80.23	81.83	88.65	89.72
sunflower	87.31	91.67	92.50	86.50	88.75	89.45	88.22	94.85	95.78
rapeseed	84.83	91.40	92.84	81.75	89.21	92.24	88.17	93.73	93.48
broad bean	78.97	82.23	86.98	72.11	76.26	82.11	87.81	89.36	92.55
shrub grass	72.55	73.83	76.36	68.68	70.79	72.68	77.00	77.28	80.50
vineyards	77.99	80.34	83.33	79.11	84.52	85.62	85.62	76.71	81.23
cherry trees	76.32	78.40	83.78	75.96	71.91	82.02	76.99	86.45	85.72
macro	81.94	85.46	87.80	80.15	83.36	86.25	84.19	88.11	89.61
weighted	85.44	89.08	90.60	85.56	89.18	90.66	85.55	89.23	90.67

In the same fashion as in Section 4.1, we run 100 experiments of the GA to acquire the most dominant features. Regarding the threshold selection, a similar behavior is observed here too, namely thresholds from 13 to 16 achieved optimum results, with the number of features ranging from 159 to 94. Table 5 illustrates also the metrics of the model trained with 120 features derived when we set a threshold of 15 ($GA_{c,15}$ model). The feature selection procedure improves even more the predictions, compared to the model trained with all features. Specifically, macro average UA, PA, and f1-score are increased by 1.5%, 2.9%, and 2.2%, respectively. Finally, in Figure 8 we show a qualitative comparison of the three models presented in Table 5, where we can observe the same pattern. The $S2_c$ only model fails to identify several cases, whereas the other two predict almost every parcel correctly.
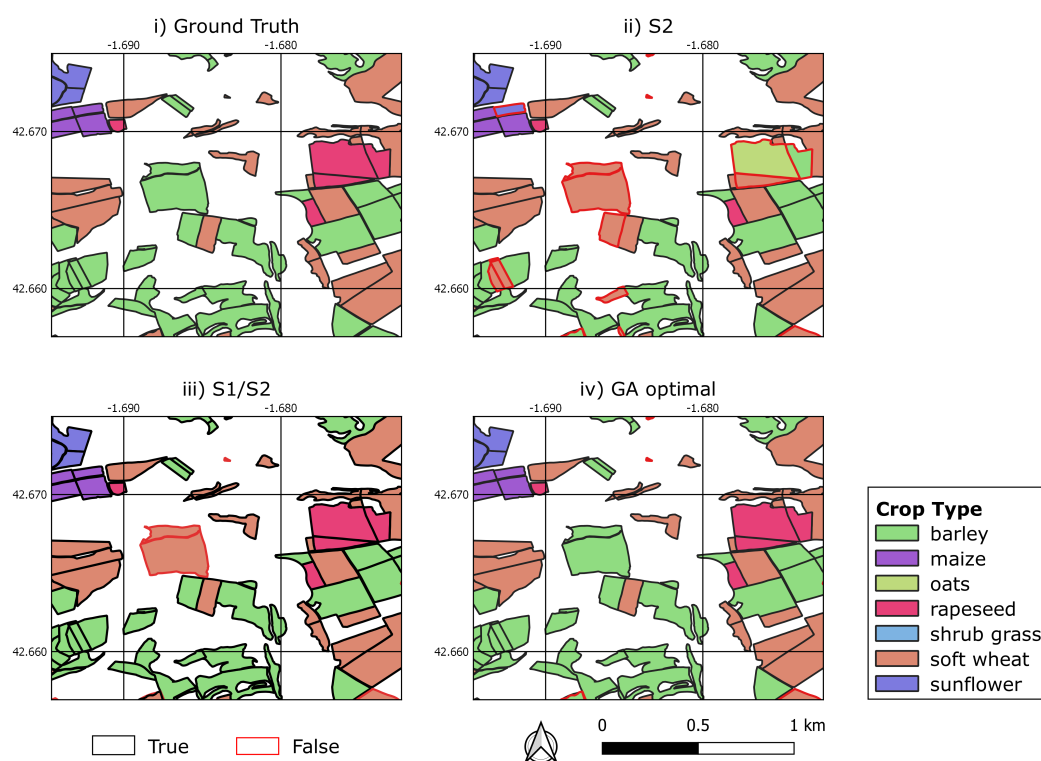
Figure 8. Crop type maps attained by the three different SVM models. (**i**) ground truth, (**ii**) predictions from the S2 model, (**iii**) predictions from the S1/S2 mode,l and (**iv**) predictions from the GA optimal model.

5. Discussion

### 5.1. Relevance of Sentinel-1 PolSAR Data for Crop Classification

Despite the recent advance in Deep Learning methods for crop classification [135,136], SVM still remains an excellent alternative. OA when using only Sentinel-2 time-series as input data is over 92%. Moreover, f1-score is more than 80% for each of the 10 different crop types, and more than 92% for half of them. This great overall performance of S2 model was expected, considering that we used high quality imagery with minimum cloud coverage and high temporal density. Although it is not fair to compare these results with studies of different areas, several recent studies achieve similar performance [18,22–24,137]. Our study verifies the value of Sentinel-2 optical images, render this type of data indispensable for achieving highly accurate crop maps.

To our knowledge, this research is the first one examining the potential of the entire set of polarimetric parameters that can be extracted using the $H/A/\bar{\alpha}$ decomposition technique in crop mapping. In Section 2.3.2, we present in detail each of the aforementioned polarimetric features. The potential of PolSAR data in identifying different crop types was assessed both alone and in synergy with optical data. Integrating multi-temporal optical and polarimetric features resulted in a very large feature space of 818 attributes. The S1 model, as expected, achieved a lower, but very promising, performance (OA more than 82%), compared to the S2 model. In terms of individual crop type metrics, the polarimetric-based SVM model fails to correctly identify the all-year crop types, but successfully manages to classify other crop types, such as rapeseed, sunflower, and maize, with class-wise metrics ranging between 90 and 95%. This is a strong indicator that polarimetric features hold important information about crops' phenology [51]. Regarding the S1/S2 model's results, even though the joint use of Sentinel-1 PolSAR and Sentinel-2 optical imagery did not have a significant impact in the OA obtained, we observed some interesting improvements in the metrics of several classes. This classification ability enhancement of certain crop types is due to the fact that PolSAR data contains enriched information about vegetation's

structural and dielectric properties that is complementary to the spectral reflectances of plants. However, SVM exhibited a worse performance in categorizing four crop types; all-year crops (cherry trees, vineyards, shrub grass), as well as oats, compared to the S2 model. This deterioration might indicate that the large feature space (818) contains several polarimetric parameters that cannot adequately describe the complex scattering processes of plants due to the fact that Sentinel-1 mission has not full polarization capabilities [64].

By utilizing GA as a feature selection module, we acquired an 80-feature subset, which included 33 polarimetric attributes. When SVM classifier was trained using, as input data, this particular mixed-type feature subset, classification accuracies were further improved. This finding not only showcases the great value of polarimetric parameters, but also highlights the effectiveness of GAs and the benefits of incorporating them as feature selection methods in crop classification tasks. Exceptional performance was also exhibited by the $GA_{c,15}$ model (i.e., the SVM trained using as input data the first 111 most important features, which were selected more than 15 times out of 100 GA runs). Figure 9 (no clouds) illustrates the relative importance of both types of data. The relative importance of each feature type was calculated, by taking into account only the features that were selected more than 10 times out of 100 GA implementations, since 10 is the minimum threshold for acquiring satisfactory classification accuracies (Figure 7). In general, the contribution of polarimetric parameters is estimated at around 25–30%, demonstrating the usefulness of PolSAR data as ancillary information in crop classification tasks.

The contribution of Sentinel-1 features is more evident in the case of adding artificial cloud noise in the original cloud-free Sentinel-2 imagery. In this scenario, the synergistic use of both optical and polarimetric data contributed to a much better discrimination of crops (OA increased more than 3.5%), compared with the S2 model. This result clearly demonstrates the great value of incorporating the cloud-penetrating PolSAR data when trying to produce accurate crop maps of agricultural areas that suffer from dense cloud cover conditions. The great usefulness of this type of data in cloudy conditions is also clearly demonstrated in Figure 9 (clouds), where the relative importance of optical and polarimetric acquire almost equal values.
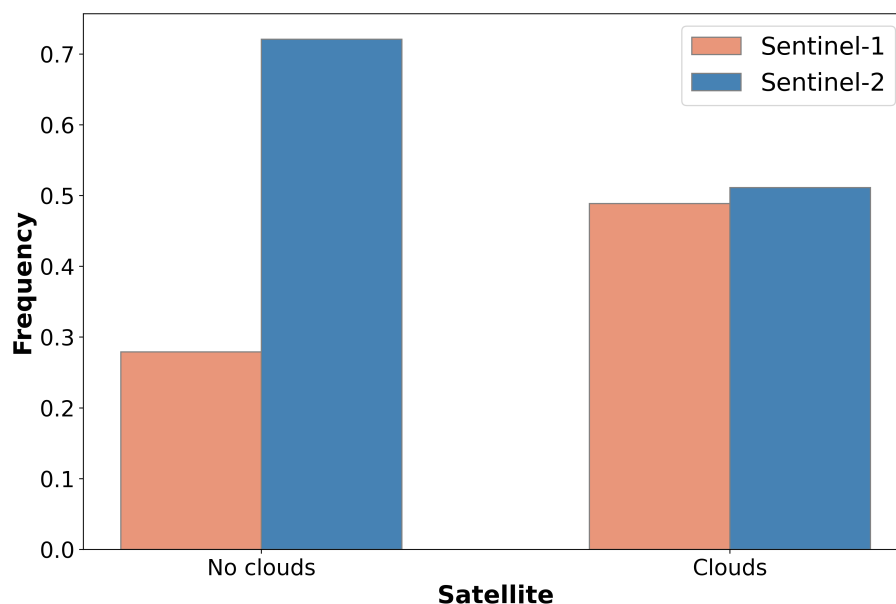
Figure 9. The aggregated importance of Sentinel-1 and Sentinel-2 features with and without clouds.

Figure 10 illustrates how the number of features of each data type changes inside the list of the most valuable attributes as the threshold t increases. This ratio-threshold relationship was examined in both scenarios of clear and artificially cloudy Sentinel-2 imagery. As it is observed, in both cases, when all individual features are considered

($t = 0$), the relative ratio of Sentinel-1 and Sentinel-2 features is 67% and 33%, respectively, as expected (see Table S1). According to Figure 10a, which refers to the original case, as the threshold increases from 0 to 7, the percentage of Sentinel-2 features gradually increases against the percentage of Sentinel-1 features, which decreases in a complementary fashion. After the threshold value of 7, where the ratios of the two types are almost equal, the Sentinel-2 data prevails, approaching a ratio of more than 95% for $t > 20$. As discussed in Section 4.1.4, for threshold values ranging between 13 and 17, SVM classifier has optimal performance. At this range, Sentinel-2 features dominate the list of the best predictors with a mean ratio of 83%. The corresponding graph in the scenario of artificial cloud masks exhibits some interesting differences (Figure 10b). As the threshold increases from 0 to 10, Sentinel-2 ratio increases with a slower rate, compared to the original case, and until $t = 25$ it present a stable behavior. At the optimal performance threshold range, the two types of features interestingly contribute in an almost equal degree. For t larger than 25, Sentinel-2 features slowly occupies a larger part of the list. However, contrary to the original case, this ratio does not surpass 80%, which indicates that the presence of polarimetric features is significant even when only a handful of features that present the highest selection frequencies are considered.


(**a**) (**b**)
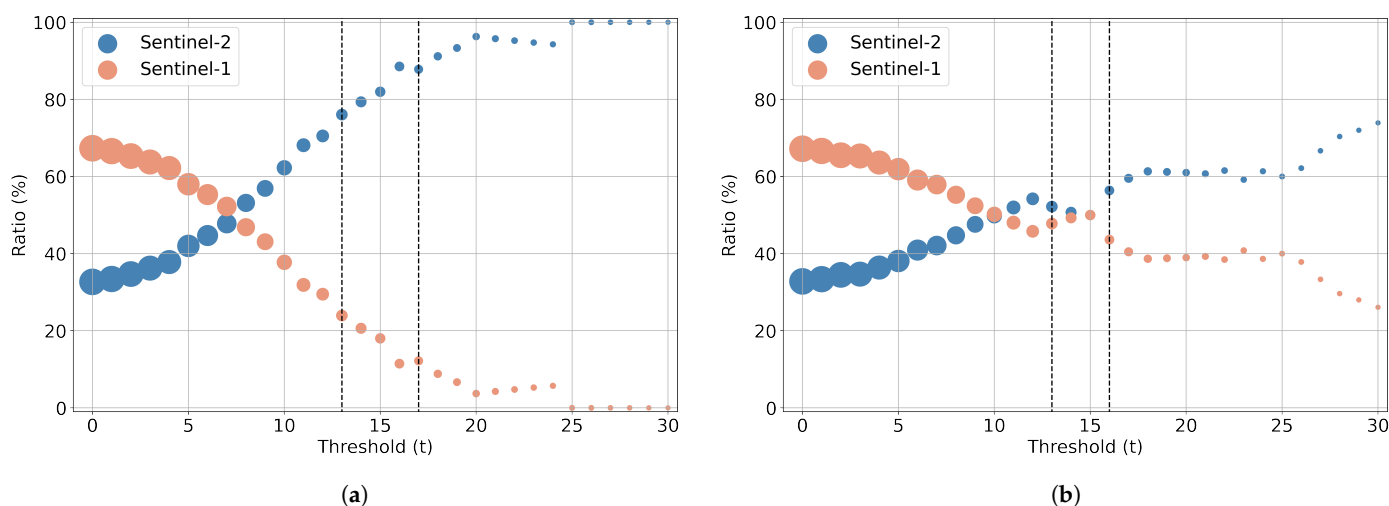
Figure 10. Evolution of the Sentinel-1 (red) and Sentinel-2 (blue) ratios inside the list of the most important features as a function of threshold value t for the original case (**a**) and the artificial clouds scenario (**b**). The size of each point corresponds to the number of features for each threshold considered. Black demarcation lines delineate the threshold range for the optimal performance of SVM classifier in each case.

5.2. Feature Importance of the Combined Sentinel-1/2 Feature Space

As discussed in Section 4.1.4, our custom GA was employed for a feature importance estimation analysis, by running multiple GA experiments and recording how many times each individual feature appeared in the optimal subset. This exhaustive and computational expensive procedure was followed in order to extract a list of the most valuable predictors with satisfactory statistical significance. Figures 11 and 12 illustrate the first 25 most important features in descending order, as recorded for the original case and the case of artificially generating clouds, respectively (the lists are available in the Supplementary Material, Tables S8 and S9). The relative importance of each feature was calculated in the same way as the importance values in Figure 9. In both cases, PSRI and NDWI were the two features with the highest relative importance. The great contribution of these particular attributes is quite reasonable, since the different crop types of this study exhibited large differences in senescence phase onset and their water content across the observation period. When the original clear Sentinel-2 imagery was used, optical features dominate the list of the 25 most important features, occupying its three quarters. Apart from

this disproportion, the optical features have generally higher relative importance values, ranging from 3.10% to 11.91%, contrary to the polarimetric features, ranging from 0.24 to 3.79%. All vegetation indices, as well as all Sentinel-2 spectral bands, are included in the most important features list, in accordance with our crop classification results in Section 4.1. This finding was expected, since optical data hold vital information about the biophysical properties of plants [22,138]. Despite the superiority of optical features, several polarimetric parameters related to Shannon entropy and to covariance matrix's eigenvalues appear significant contribution. Concerning the second scenario, the presence of artificial clouds in the Sentinel-2 imagery revealed the hidden value of PolSAR data. Shannon entropy, second eigenvalue, as well as the normalised Shannon entropy were placed among the top 5 features, followed by Shannon entropy intensity and the normalised value of Shannon entropy intensity in positions 7 and 8, respectively. Moreover, there is almost a balance between the number of two types of features. These results are verified by the findings of recent publications [49–52,63], which clearly demonstrate the great potential of Shannon entropy, entropy and mean alpha angle in crop monitoring, and crop classification.

Apart from this analysis, we also performed an importance analysis for each month of the observation period both for the original case and the case of artificially cloudy images. The relative importance value of each month was calculated in the same fashion as in features' relative importance analysis. As illustrated in Figure 13, in both cases, July is the month with the greater contribution. July's high competence can be interpreted, considering that, during this month, summer and winder crops are going through a different stage of development (inflorescence and maturation, respectively) [137] and, as a result, present large differences in biophysical and structural properties. For the original case, June and April are the second and third most informative months, respectively. According to Figure 2, June is a transitional period in crops' growth cycle, since winter crops gradually approaching their full development and summer crops pass into their flowering stage. Additionally, April is the sowing period of summer crops and the flowering phase of winter crops and, thus, this month is vital for their accurate discrimination. This order is different for the second scenario of using artificially generated cloud masks, where May and June are the following most important months. The significant decrease in April's relative importance might be explained, considering that valuable information content is missed due to the addition of artificial cloud noise. Despite these differences, for the majority of months, feature importance values do not present significant changes for the two scenarios examined. We also observe an important contribution of features acquired during January, which is almost doubled for the case of artificial clouds and on the other hand a very low contribution of February. These two months are useful for identifying the all-year crop types and potentially some winter crops. Normally, we would expect both these months to contribute equally, however from Figure 2 we observe that there are no available cloud-free Sentinel-2 images during February. Moreover, if we look at Tables S8 and S9 in the Supplementary Material we notice that Sentinel-2 features during January are among the most important ones and contribute more often that the Sentinel-1 from either January or February. Based on that, we assume that the information about the crops during this 2-month period is mostly captured from the Sentinel-2 features derived in late January and the rest of the Sentinel-1 features in February are redundant and do not boost the classification performance.
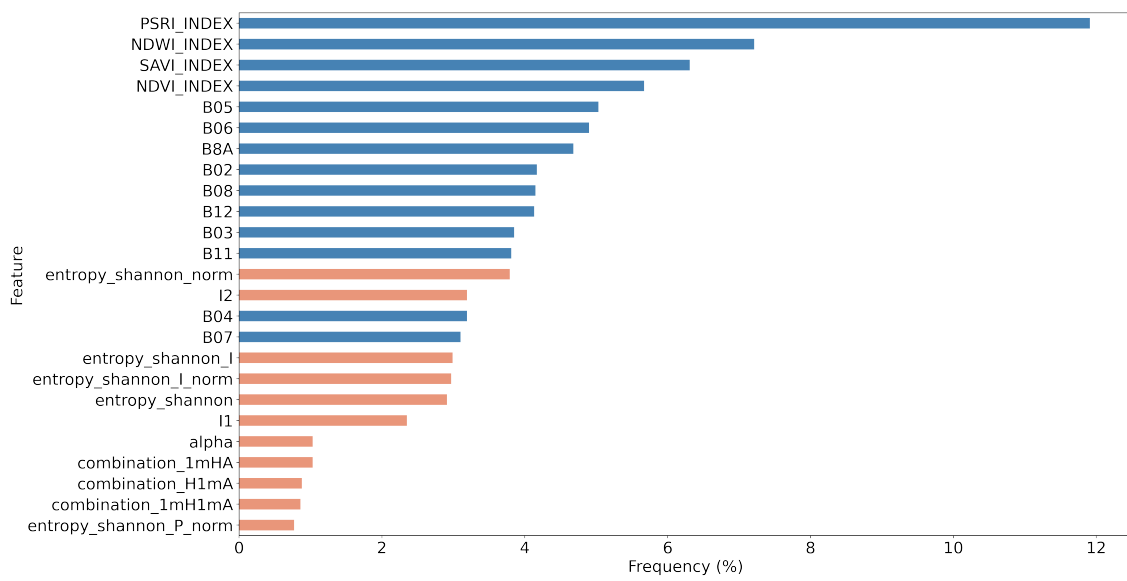
Figure 11. Feature importance of each feature without clouds. Blue indicates Sentinel-2 and orange Sentinel-1 features.
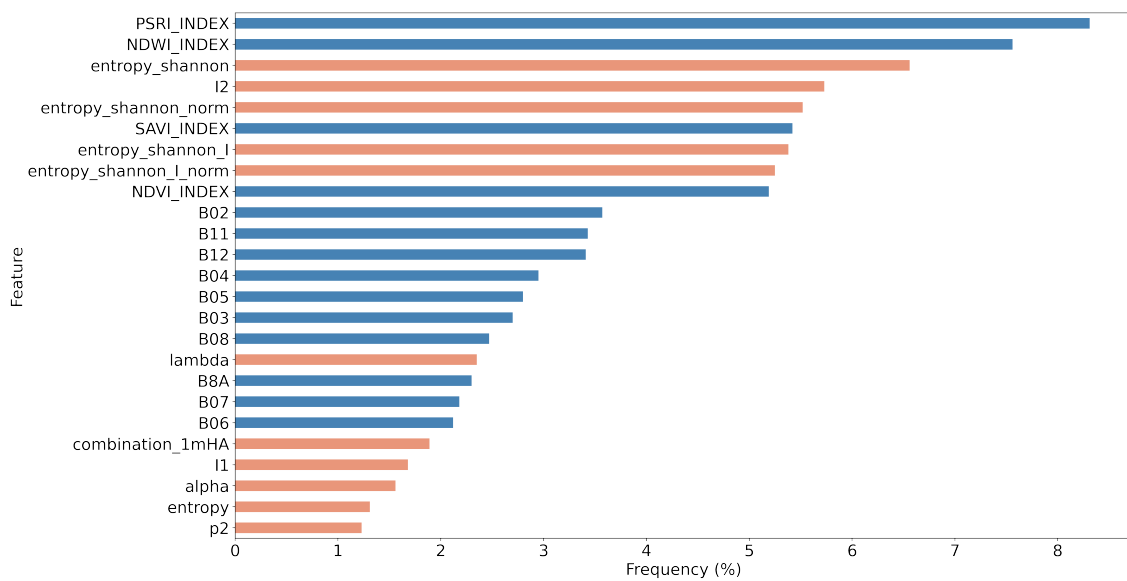
Figure 12. Feature importance of each feature with clouds. Blue indicates Sentinel-2 and orange Sentinel-1 features.
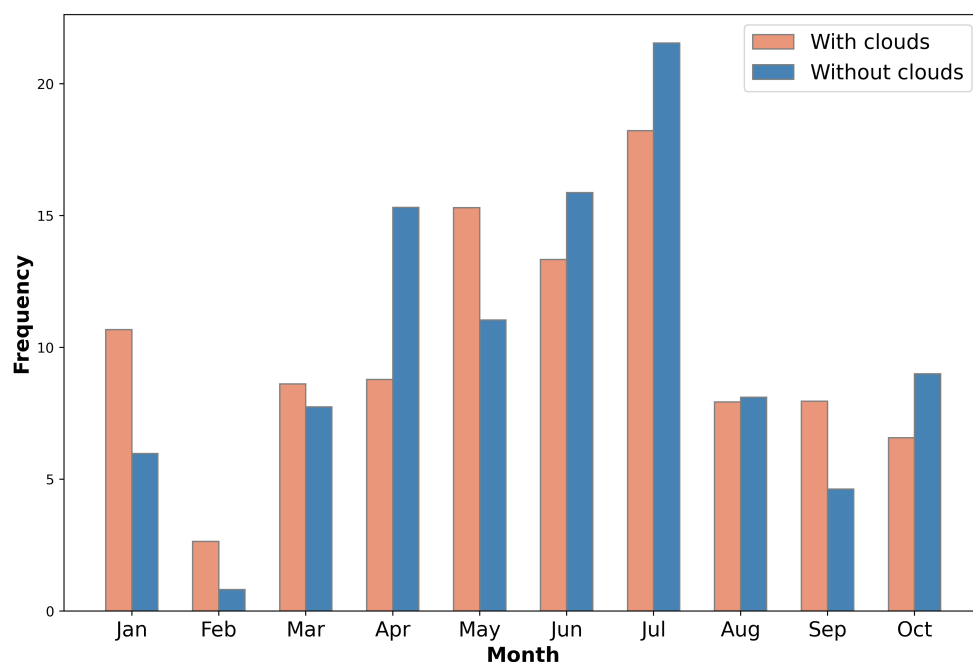
Figure 13. Feature importance of each month with and without clouds.

5.3. Comparison of the GA with Other Feature Selection Methods

In order to further validate GA's effectiveness as a feature selection method, we examined the performance of other well known and widely used feature selection algorithms, namely Mutual Regression (MR) [139,140], coefficients of Lasso, feature importance of Random Forest (RF) and Recursive Feature Elimination (RFE) by recursively training RF and discard the less important features in each iteration. Table 6 presents the OA and the macro-averaged f1-score for both cases (with and without the addition of artificial clouds). GA achieves the best performance in both scenarios and, especially, in the case of artificial clouds, where the f1 score is more than 1.5% higher than any other method. These experimental results underline GA's efficiency and robustness, as well as its superiority compared to other feature selection modules.

Table 6. Performance of the different feature selection methods. Bold indicates the methods with which the best results are achieved.

	No Clouds			Clouds		
Selection Method	#Features	OA	f1 Macro	#Features	OA	f1 Macro
MR	111	92.63	89.81	120	87.72	83.54
RFE	111	93.54	91.19	120	89.38	85.85
Lasso	111	93.83	91.60	120	89.83	86.03
RF	111	93.18	90.59	120	88.36	83.86
GA	111	**94.00**	**91.75**	120	**90.66**	**87.80**

5.4. Limitations

It should be pointed out that this work comes with some limitations. Since we did not have actual ground truth data, we assume the validity of farmers' declarations to train and evaluate our models. Even though the declarations in Navarra are expected to be ∼97% accurate [19], still this can affect to a small degree the training and evaluation process. Additionally, the proposed methodology has been applied only to a specific area for a specific year and it should be tested in areas of different agroclimatic characteristics and for different inspection years to evaluate its generalization capabilities. Finally, the production of the polarimetric features is a very time-consuming procedure and, therefore, applying

the proposed pipeline from scratch in another area requires a lot of computational time. However, we partially mitigate this limitation by proposing to use only a handful of useful polarimetric features, for the task at hand, based on our analysis.

6. Conclusions

In this paper, a large number of multi-temporal Sentinel-1 and Sentinel-2 dual-PolSAR features (818) were incorporated into various SVM classification scenarios in order to obtain high-quality crop-type maps of an agricultural region located in Navarre, Spain. One of the main contributions of this work is the assessment of the full set of 23 different polarimetric parameters that can be extracted, by applying Cloude–Pottier decomposition technique available at the PolSARpro software, for the task of crop classification. Moreover, a custom GA has been implemented and utilized as a feature selection method to derive an optimal feature subset out of the high dimensional feature space, as well as to perform a feature importance analysis for acquiring the most informative features. Aiming to examine the added value of PolSAR data, as well as the effectiveness of GAs, we trained and evaluated numerous classification models by making use of the available mixed-type features and GA's outputs. The main conclusions of the study come be summed up to the following:

1. The use of all the available optical and polarimetric features improved slightly the crop classification accuracy. However, when artificial cloud masks were injected into the original Sentinel-2 imagery, simulating a real world scenario, the added value of PolSAR data was revealed. The corresponding polarimetric/optical synergistic SVM model presented an accuracy improvement of more than 3.5%, in comparison with the optical-based model under artificially cloudy conditions. This experimental result showcases the potential value of this approach in relevant tasks above agricultural regions that suffer from frequent cloud cover.
2. By employing our custom GA, we re-identified the most important features in the scenario of artificial clouds and used them an input data in the SVM classifier. This particular model exhibited an increased OA by 1.5%, approaching 90.66%.
3. Through a computationally demanding feature importance estimation analysis of carrying out more than 100 GA experiments, we derived a sorted list of the most important individual predictors in both scenarios of the original cloud-free Sentinel-2 dataset and the one with the artificial cloud masks that could be effectively utilized in future studies. This feature importance analysis verified the great contribution of Sentinel-2 attributes in the original case, as expected, and highlighted the great relative importance of several polarimetric SAR parameters, such as Shannon entropy, especially in the case of injecting artificial cloud coverage.

Conflicts of Interest: The authors declare no conflicts of interest.

References

1. Larrañaga, A.; Álvarez-Mozos, J. On the added value of quad-pol data in a multi-temporal crop classification framework based on RADARSAT-2 imagery. *Remote Sens.* **2016**, *8*, 335. [CrossRef]
2. Orynbaikyzy, A.; Gessner, U.; Conrad, C. Crop type classification using a combination of optical and radar remote sensing data: A review. *Int. J. Remote Sens.* **2019**, *40*, 6553–6595. [CrossRef]
3. Dakir, A.; Alami, O.B.; Barramou, F. Crop type mapping using optical and radar images: A review. In Proceedings of the 2020 IEEE International conference of Moroccan Geomatics (Morgeo), Casablanca, Morocco, 11–13 May 2020; pp. 1–8.
4. Sonobe, R.; Tani, H.; Wang, X.; Kobayashi, N.; Shimamura, H. Discrimination of crop types with TerraSAR-X-derived information. *Phys. Chem. Earth Parts A/B/C* **2015**, *83*, 2–13. [CrossRef]
5. Giannarakis, G.; Sitokonstantinou, V.; Lorilla, R.S.; Kontoes, C. Towards assessing agricultural land suitability with causal machine learning. In Proceedings of the 2022 IEEE/CVF Conference on Computer Vision and Pattern Recognition Workshops (CVPRW), New Orleans, LA, USA, 19–20 June 2022; pp. 1442–1452.
6. Sishodia, R.P.; Ray, R.L.; Singh, S.K. Applications of remote sensing in precision agriculture: A review. *Remote Sens.* **2020**, *12*, 3136. [CrossRef]
7. Phiri, D.; Simwanda, M.; Salekin, S.; Nyirenda, V.R.; Murayama, Y.; Ranagalage, M. Sentinel-2 data for land cover/use mapping: A review. *Remote Sens.* **2020**, *12*, 2291. [CrossRef]
8. Campos-Taberner, M.; García-Haro, F.J.; Martínez, B.; Sánchez-Ruíz, S.; Gilabert, M.A. A copernicus Sentinel-1 and Sentinel-2 classification framework for the 2020+ European common agricultural policy: A case study in València (Spain). *Agronomy* **2019**, *9*, 556. [CrossRef]
9. Beriaux, E.; Jago, A.; Lucau-Danila, C.; Planchon, V.; Defourny, P. Sentinel-1 Time Series for Crop Identification in the Framework of the Future CAP Monitoring. *Remote Sens.* **2021**, *13*, 2785. [CrossRef]
10. Hunt, M.L.; Blackburn, G.A.; Carrasco, L.; Redhead, J.W.; Rowland, C.S. High resolution wheat yield mapping using Sentinel-2. *Remote Sens. Environ.* **2019**, *233*, 111410. [CrossRef]
11. Nasirzadehdizaji, R.; Balik Sanli, F.; Abdikan, S.; Cakir, Z.; Sekertekin, A.; Ustuner, M. Sensitivity analysis of multi-temporal Sentinel-1 SAR parameters to crop height and canopy coverage. *Appl. Sci.* **2019**, *9*, 655. [CrossRef]
12. Torres, R.; Snoeij, P.; Geudtner, D.; Bibby, D.; Davidson, M.; Attema, E.; Potin, P.; Rommen, B.; Floury, N.; Brown, M.; et al. GMES Sentinel-1 mission. *Remote Sens. Environ.* **2012**, *120*, 9–24. [CrossRef]
13. Raspini, F.; Bianchini, S.; Ciampalini, A.; Del Soldato, M.; Solari, L.; Novali, F.; Del Conte, S.; Rucci, A.; Ferretti, A.; Casagli, N. Continuous, semi-automatic monitoring of ground deformation using Sentinel-1 satellites. *Sci. Rep.* **2018**, *8*, 7253. [CrossRef]
14. Van Tricht, K.; Gobin, A.; Gilliams, S.; Piccard, I. Synergistic use of radar Sentinel-1 and optical Sentinel-2 imagery for crop mapping: A case study for Belgium. *Remote Sens.* **2018**, *10*, 1642. [CrossRef]
15. Lechner, A.M.; Foody, G.M.; Boyd, D.S. Applications in remote sensing to forest ecology and management. *One Earth* **2020**, *2*, 405–412. [CrossRef]
16. Gao, H.; Wang, C.; Wang, G.; Zhu, J.; Tang, Y.; Shen, P.; Zhu, Z. A crop classification method integrating GF-3 PolSAR and Sentinel-2A optical data in the Dongting Lake Basin. *Sensors* **2018**, *18*, 3139. [CrossRef]
17. Kobayashi, N.; Tani, H.; Wang, X.; Sonobe, R. Crop classification using spectral indices derived from Sentinel-2A imagery. *J. Inf. Telecommun.* **2020**, *4*, 67–90. [CrossRef]
18. Mazzia, V.; Khaliq, A.; Chiaberge, M. Improvement in land cover and crop classification based on temporal features learning from Sentinel-2 data using recurrent-convolutional neural network (R-CNN). *Appl. Sci.* **2019**, *10*, 238. [CrossRef]
19. Sitokonstantinou, V.; Papoutsis, I.; Kontoes, C.; Lafarga Arnal, A.; Armesto Andrés, A.P.; Garraza Zurbano, J.A. Scalable parcel-based crop identification scheme using Sentinel-2 data time-series for the monitoring of the common agricultural policy. *Remote Sens.* **2018**, *10*, 911. [CrossRef]
20. Sitokonstantinou, V.; Koukos, A.; Drivas, T.; Kontoes, C.; Papoutsis, I.; Karathanassi, V. A Scalable Machine Learning Pipeline for Paddy Rice Classification Using Multi-Temporal Sentinel Data. *Remote Sens.* **2021**, *13*, 1769. [CrossRef]
21. Sitokonstantinou, V.; Drivas, T.; Koukos, A.; Papoutsis, I.; Kontoes, C. Scalable distributed random forest classification for paddy rice mapping. *Zenodo* **2020**, *11* . [CrossRef]
22. Yi, Z.; Jia, L.; Chen, Q. Crop classification using multi-temporal Sentinel-2 data in the Shiyang River Basin of China. *Remote Sens.* **2020**, *12*, 4052. [CrossRef]
23. Rußwurm, M.; Körner, M. Multi-temporal land cover classification with sequential recurrent encoders. *ISPRS Int. J. Geo-Inf.* **2018**, *7*, 129. [CrossRef]

24. Jiang, Y.; Lu, Z.; Li, S.; Lei, Y.; Chu, Q.; Yin, X.; Chen, F. Large-scale and high-resolution crop mapping in china using Sentinel-2 satellite imagery. *Agriculture* **2020**, *10*, 433. [CrossRef]

25. Chen, Y.; Lu, D.; Moran, E.; Batistella, M.; Dutra, L.V.; Sanches, I.D.; da Silva, R.F.B.; Huang, J.; Luiz, A.J.B.; de Oliveira, M.A.F. Mapping croplands, cropping patterns, and crop types using MODIS time-series data. *Int. J. Appl. Earth Obs. Geoinf.* **2018**, *69*, 133–147. [CrossRef]

26. Liu, C.a.; Chen, Z.X.; Yun, S.; Chen, J.s.; Hasi, T.; PAN, H.z. Research advances of SAR remote sensing for agriculture applications: A review. *J. Integr. Agric.* **2019**, *18*, 506–525. [CrossRef]

27. Valcarce-Diñeiro, R.; Arias-Pérez, B.; Lopez-Sanchez, J.M.; Sánchez, N. Multi-temporal dual-and quad-polarimetric synthetic aperture radar data for crop-type mapping. *Remote Sens.* **2019**, *11*, 1518. [CrossRef]

28. Mandal, D.; Kumar, V.; Ratha, D.; Dey, S.; Bhattacharya, A.; Lopez-Sanchez, J.M.; McNairn, H.; Rao, Y.S. Dual polarimetric radar vegetation index for crop growth monitoring using Sentinel-1 SAR data. *Remote Sens. Environ.* **2020**, *247*, 111954. [CrossRef]

29. Arias, M.; Campo-Bescós, M.Á.; Álvarez-Mozos, J. Crop classification based on temporal signatures of Sentinel-1 observations over Navarre province, Spain. *Remote Sens.* **2020**, *12*, 278. [CrossRef]

30. Mestre-Quereda, A.; Lopez-Sanchez, J.M.; Vicente-Guijalba, F.; Jacob, A.W.; Engdahl, M.E. Time-series of Sentinel-1 interferometric coherence and backscatter for crop-type mapping. *IEEE J. Sel. Top. Appl. Earth Obs. Remote Sens.* **2020**, *13*, 4070–4084. [CrossRef]

31. Zhu, X.X.; Montazeri, S.; Ali, M.; Hua, Y.; Wang, Y.; Mou, L.; Shi, Y.; Xu, F.; Bamler, R. Deep learning meets SAR: Concepts, models, pitfalls, and perspectives. *IEEE Geosci. Remote Sens. Mag.* **2021**, *9*, 143–172. [CrossRef]

32. Qu, Y.; Zhao, W.; Yuan, Z.; Chen, J. Crop Mapping from Sentinel-1 Polarimetric Time-Series with a Deep Neural Network. *Remote Sens.* **2020**, *12*, 2493. [CrossRef]

33. Lee, J.S.; Pottier, E. *Polarimetric Radar Imaging: From Basics to Applications*; CRC Press: Boca Raton, FL, USA, 2017.

34. Ustuner, M.; Balik Sanli, F. Polarimetric target decompositions and light gradient boosting machine for crop classification: A comparative evaluation. *ISPRS Int. J. Geo-Inf.* **2019**, *8*, 97. [CrossRef]

35. Cloude, S.R.; Pottier, E. An entropy based classification scheme for land applications of polarimetric SAR. *IEEE Trans. Geosci. Remote Sens.* **1997**, *35*, 68–78. [CrossRef]

36. Zeyada, H.H.; Ezz, M.M.; Nasr, A.H.; Shokr, M.; Harb, H.M. Evaluation of the discrimination capability of full polarimetric SAR data for crop classification. *Int. J. Remote Sens.* **2016**, *37*, 2585–2603. [CrossRef]

37. Cloude, S. The dual polarization entropy/alpha decomposition: A PALSAR case study. *Sci. Appl. SAR Polarim. Polarim. Interferom.* **2007**, *644*, 2.

38. Ouchi, K. Recent trend and advance of synthetic aperture radar with selected topics. *Remote Sens.* **2013**, *5*, 716–807. [CrossRef]

39. López-Martínez, C.; Pottier, E. Basic principles of SAR polarimetry. In *Polarimetric Synthetic Aperture Radar*; Springer: Berlin/Heidelberg, Germany, 2021; pp. 1–58.

40. Pottier, E.; Sarti, F.; Fitrzyk, M.; Patruno, J. PolSARpro-Biomass Edition: The new ESA polarimetric SAR data processing and educational toolbox for the future ESA & third party fully polarimetric SAR missions. In Proceedings of the ESA Living Planet Symposium 2019, Milan, Italy, 13–17 May 2019.

41. Morio, J.; Réfrégier, P.; Goudail, F.; Dubois-Fernandez, P.; Dupuis, X. Application of information theory measures to polarimetric and interferometric SAR images. In Proceedings of the PSIP 2007—5th International Conference on Physics in Signal & Image Processing, Mulhouse, France, 30 January–2 February 2007.

42. Li, M.; Bijker, W. Vegetable classification in Indonesia using Dynamic Time Warping of Sentinel-1A dual polarization SAR time series. *Int. J. Appl. Earth Obs. Geoinf.* **2019**, *78*, 268–280. [CrossRef]

43. Sayedain, S.A.; Maghsoudi, Y.; Eini-Zinab, S. Assessing the use of cross-orbit Sentinel-1 images in land cover classification. *Int. J. Remote Sens.* **2020**, *41*, 7801–7819. [CrossRef]

44. Diniz, J.M.F.d.S.; Gama, F.F.; Adami, M. Evaluation of polarimetry and interferometry of Sentinel-1A SAR data for land use and land cover of the Brazilian Amazon Region. *Geocarto Int.* **2022**, *37*, 1482–1500. [CrossRef]

45. Whyte, A.; Ferentinos, K.P.; Petropoulos, G.P. A new synergistic approach for monitoring wetlands using Sentinels-1 and 2 data with object-based machine learning algorithms. *Environ. Model. Softw.* **2018**, *104*, 40–54. [CrossRef]

46. Hu, J.; Ghamisi, P.; Zhu, X.X. Feature extraction and selection of Sentinel-1 dual-pol data for global-scale local climate zone classification. *ISPRS Int. J. Geo-Inf.* **2018**, *7*, 379. [CrossRef]

47. Schulz, D.; Yin, H.; Tischbein, B.; Verleysdonk, S.; Adamou, R.; Kumar, N. Land use mapping using Sentinel-1 and Sentinel-2 time series in a heterogeneous landscape in Niger, Sahel. *ISPRS J. Photogramm. Remote Sens.* **2021**, *178*, 97–111. [CrossRef]

48. Harfenmeister, K.; Itzerott, S.; Weltzien, C.; Spengler, D. Agricultural monitoring using polarimetric decomposition parameters of Sentinel-1 data. *Remote Sens.* **2021**, *13*, 575. [CrossRef]

49. Mercier, A.; Betbeder, J.; Baudry, J.; Le Roux, V.; Spicher, F.; Lacoux, J.; Roger, D.; Hubert-Moy, L. Evaluation of Sentinel-1 & 2 time series for predicting wheat and rapeseed phenological stages. *ISPRS J. Photogramm. Remote Sens.* **2020**, *163*, 231–256.

50. Haldar, D.; Verma, A.; Kumar, S.; Chauhan, P. Estimation of mustard and wheat phenology using multi-date Shannon entropy and Radar Vegetation Index from polarimetric Sentinel-1. *Geocarto Int.* **2021**, *37*, 1–22. [CrossRef]

51. Yeasin, M.; Haldar, D.; Kumar, S.; Paul, R.K.; Ghosh, S. Machine Learning Techniques for Phenology Assessment of Sugarcane Using Conjunctive SAR and Optical Data. *Remote Sens.* **2022**, *14*, 3249. [CrossRef]

52. Mercier, A.; Betbeder, J.; Rapinel, S.; Jegou, N.; Baudry, J.; Hubert-Moy, L. Evaluation of Sentinel-1 and-2 time series for estimating LAI and biomass of wheat and rapeseed crop types. *J. Appl. Remote Sens.* **2020**, *14*, 024512. [CrossRef]

53. Umutoniwase, N.; Lee, S.K. The Potential of Sentinel-1 SAR Parameters in Monitoring Rice Paddy Phenological Stages in Gimhae, South Korea. *Korean J. Remote Sens.* **2021**, *37*, 789–802.

54. Hosseini, M.; Becker-Reshef, I.; Sahajpal, R.; Lafluf, P.; Leale, G.; Puricelli, E.; Skakun, S.; McNairn, H. Soybean Yield Forecast Using Dual-Polarimetric C-Band Synthetic Aperture Radar. *ISPRS Ann. Photogramm. Remote Sens. Spat. Inf. Sci.* **2022**, *3*, 405–410. [CrossRef]

55. De Petris, S.; Sarvia, F.; Gullino, M.; Tarantino, E.; Borgogno-Mondino, E. Sentinel-1 polarimetry to map apple orchard damage after a storm. *Remote Sens.* **2021**, *13*, 1030. [CrossRef]

56. Elkharrouba, E.; Sekertekin, A.; Fathi, J.; Tounsi, Y.; Bioud, H.; Nassim, A. Surface soil moisture estimation using dual-Polarimetric Stokes parameters and backscattering coefficient. *Remote Sens. Appl. Soc. Environ.* **2022**, *26*, 100737. [CrossRef]

57. Tavus, B.; Kocaman, S.; Nefeslioglu, H.; Gokceoglu, C. A fusion approach for flood mapping using Sentinel-1 and Sentinel-2 datasets. *Int. Arch. Photogramm. Remote Sens. Spat. Inf. Sci.* **2020**, *43*, 641–648. [CrossRef]

58. Parida, B.R.; Mandal, S.P. Polarimetric decomposition methods for LULC mapping using ALOS L-band PolSAR data in Western parts of Mizoram, Northeast India. *SN Appl. Sci.* **2020**, *2*, 1049. [CrossRef]

59. Wang, D.; Liu, C.A.; Zeng, Y.; Tian, T.; Sun, Z. Dryland Crop Classification Combining Multitype Features and Multitemporal Quad-Polarimetric RADARSAT-2 Imagery in Hebei Plain, China. *Sensors* **2021**, *21*, 332. [CrossRef]

60. Sun, Z.; Wang, D.; Zhong, G. A review of crop classification using satellite-based polarimetric SAR imagery. In Proceedings of the 2018 7th International Conference on Agro-Geoinformatics (Agro-Geoinformatics), Hangzhou, China, 6–9 August 2018; pp. 1–5.

61. Guo, J.; Wei, P.L.; Liu, J.; Jin, B.; Su, B.F.; Zhou, Z.S. Crop Classification Based on Differential Characteristics of H/α Scattering Parameters for Multitemporal Quad-and Dual-Polarization SAR Images. *IEEE Trans. Geosci. Remote Sens.* **2018**, *56*, 6111–6123. [CrossRef]

62. Kpienbaareh, D.; Sun, X.; Wang, J.; Luginaah, I.; Bezner Kerr, R.; Lupafya, E.; Dakishoni, L. Crop type and land cover mapping in northern Malawi using the integration of Sentinel-1, Sentinel-2, and planetscope satellite data. *Remote Sens.* **2021**, *13*, 700. [CrossRef]

63. Denize, J.; Hubert-Moy, L.; Pottier, E. Polarimetric SAR time-series for identification of winter land use. *Sensors* **2019**, *19*, 5574. [CrossRef]

64. Gella, G.W.; Bijker, W.; Belgiu, M. Mapping crop types in complex farming areas using SAR imagery with dynamic time warping. *ISPRS J. Photogramm. Remote Sens.* **2021**, *175*, 171–183. [CrossRef]

65. Gao, H.; Wang, C.; Wang, G.; Li, Q.; Zhu, J. A new crop classification method based on the time-varying feature curves of time series dual-polarization Sentinel-1 data sets. *IEEE Geosci. Remote Sens. Lett.* **2019**, *17*, 1183–1187. [CrossRef]

66. Oldoni, L.; Prudente, V.; Diniz, J.; Wiederkehr, N.; Sanches, I.; Gama, F. Polarimetric Sar Data from Sentinel-1A Applied to Early Crop Classification. *Int. Arch. Photogramm. Remote Sens. Spat. Inf. Sci.* **2020**, *43*, 1039–1046. [CrossRef]

67. Gao, H.; Wang, C.; Wang, G.; Fu, H.; Zhu, J. A novel crop classification method based on ppfSVM classifier with time-series alignment kernel from dual-polarization SAR datasets. *Remote Sens. Environ.* **2021**, *264*, 112628. [CrossRef]

68. Chabalala, Y.; Adam, E.; Ali, K.A. Machine Learning Classification of Fused Sentinel-1 and Sentinel-2 Image Data towards Mapping Fruit Plantations in Highly Heterogenous Landscapes. *Remote Sens.* **2022**, *14*, 2621. [CrossRef]

69. Yaping, D.; Zhongxin, C. A review of crop identification and area monitoring based on SAR image. In Proceedings of the 2012 First International Conference on Agro-Geoinformatics (Agro-Geoinformatics), Shanghai, China, 2–4 August 2012; pp. 1–4.

70. Chakhar, A.; Hernández-López, D.; Ballesteros, R.; Moreno, M.A. Improving the accuracy of multiple algorithms for crop classification by integrating Sentinel-1 observations with Sentinel-2 data. *Remote Sens.* **2021**, *13*, 243. [CrossRef]

71. David, N.; Giordano, S.; Mallet, C. Investigating operational country-level crop monitoring with Sentinel-1 and -2 imagery. *Remote Sens. Lett.* **2021**, *12*, 970–982. [CrossRef]

72. Kussul, N.; Lavreniuk, M.; Shumilo, L. Deep Recurrent Neural Network for Crop Classification Task Based on Sentinel-1 and Sentinel-2 Imagery. In Proceedings of the IGARSS 2020–2020 IEEE International Geoscience and Remote Sensing Symposium, Waikoloa, HI, USA, 26 September–2 October 2020; pp. 6914–6917.

73. Niculescu Sr, S.; Billey, A.; Talab-Ou-Ali, H., Jr. Random forest classification using Sentinel-1 and Sentinel-2 series for vegetation monitoring in the Pays de Brest (France). In Proceedings of the SPIE Remote Sensing for Agriculture, Ecosystems, and Hydrology XX, Berlin, Germany, 10–13 September 2018; Volume 10783, p. 1078305.

74. Felegari, S.; Sharifi, A.; Moravej, K.; Amin, M.; Golchin, A.; Muzirafuti, A.; Tariq, A.; Zhao, N. Integration of Sentinel 1 and Sentinel 2 Satellite Images for Crop Mapping. *Appl. Sci.* **2021**, *11*, 10104. [CrossRef]

75. Fundisi, E.; Tesfamichael, S.G.; Ahmed, F. A combination of Sentinel-1 RADAR and Sentinel-2 multispectral data improves classification of morphologically similar savanna woody plants. *Eur. J. Remote Sens.* **2022**, *55*, 372–387. [CrossRef]

76. He, T.; Zhao, K. Multispectral remote sensing land use classification based on RBF neural network with parameters optimized by genetic algorithm. In Proceedings of the 2018 International Conference on Sensor Networks and Signal Processing (SNSP), Xi'an, China, 28–31 October 2018; pp. 118–123.

77. Chu, H.; Ge, L.; Ng, A.; Rizos, C. Application of genetic algorithm and support vector machine in classification of multisource remote sensing data. *Int. J. Remote Sens. Appl.* **2012**, *2*, 1–11.

78. Zhu, J.; Pan, Z.; Wang, H.; Huang, P.; Sun, J.; Qin, F.; Liu, Z. An improved multi-temporal and multi-feature tea plantation identification method using Sentinel-2 imagery. *Sensors* **2019**, *19*, 2087. [CrossRef]

79. Cui, J.; Zhang, X.; Wang, W.; Wang, L. Integration of optical and SAR remote sensing images for crop-type mapping based on a novel object-oriented feature selection method. *Int. J. Agric. Biol. Eng.* **2020**, *13*, 178–190. [CrossRef]

80. Paul, S.; Kumar, D.N. Evaluation of feature selection and feature extraction techniques on multi-temporal Landsat-8 images for crop classification. *Remote Sens. Earth Syst. Sci.* **2019**, *2*, 197–207. [CrossRef]

81. Blickensdörfer, L.; Schwieder, M.; Pflugmacher, D.; Nendel, C.; Erasmi, S.; Hostert, P. Mapping of crop types and crop sequences with combined time series of Sentinel-1, Sentinel-2 and Landsat 8 data for Germany. *Remote Sens. Environ.* **2022**, *269*, 112831. [CrossRef]

82. Löw, F.; Michel, U.; Dech, S.; Conrad, C. Impact of feature selection on the accuracy and spatial uncertainty of per-field crop classification using support vector machines. *ISPRS J. Photogramm. Remote Sens.* **2013**, *85*, 102–119. [CrossRef]

83. Yin, L.; You, N.; Zhang, G.; Huang, J.; Dong, J. Optimizing feature selection of individual crop types for improved crop mapping. *Remote Sens.* **2020**, *12*, 162. [CrossRef]

84. Wirsansky, E. *Hands-On Genetic Algorithms with Python: Applying Genetic Algorithms to Solve Real-World Deep Learning and Artificial Intelligence Problems*; Packt Publishing Ltd.: Birmingham, UK, 2020.

85. Zhi, H.; Liu, S. Face recognition based on genetic algorithm. *J. Vis. Commun. Image Represent.* **2019**, *58*, 495–502. [CrossRef]

86. Kramer, O. Genetic algorithms. In *Genetic Algorithm Essentials*; Springer: Berlin/Heidelberg, Germany, 2017; pp. 11–19.

87. Haddadi G.A.; Reza Sahebi, M.; Mansourian, A. Polarimetric SAR feature selection using a genetic algorithm. *Can. J. Remote Sens.* **2011**, *37*, 27–36. [CrossRef]

88. Li, S.; Wu, H.; Wan, D.; Zhu, J. An effective feature selection method for hyperspectral image classification based on genetic algorithm and support vector machine. *Knowl.-Based Syst.* **2011**, *24*, 40–48. [CrossRef]

89. Shi, L.; Wan, Y.; Gao, X.; Wang, M. Feature selection for object-based classification of high-resolution remote sensing images based on the combination of a genetic algorithm and tabu search. *Comput. Intell. Neurosci.* **2018**, *2018*, 6595792. [CrossRef]

90. Zhou, Y.; Zhang, R.; Wang, S.; Wang, F. Feature selection method based on high-resolution remote sensing images and the effect of sensitive features on classification accuracy. *Sensors* **2018**, *18*, 2013. [CrossRef]

91. Zhuo, L.; Zheng, J.; Li, X.; Wang, F.; Ai, B.; Qian, J. A genetic algorithm based wrapper feature selection method for classification of hyperspectral images using support vector machine. In Proceedings of the Geoinformatics 2008 and Joint Conference on GIS and Built Environment: Classification of Remote Sensing Images, Guangzhou, China, 28–29 June 2008; Volume 7147, pp. 503–511.

92. Ming, D.; Zhou, T.; Wang, M.; Tan, T. Land cover classification using random forest with genetic algorithm-based parameter optimization. *J. Appl. Remote Sens.* **2016**, *10*, 035021. [CrossRef]

93. Tomppo, E.; Antropov, O.; Praks, J. Cropland classification using Sentinel-1 time series: Methodological performance and prediction uncertainty assessment. *Remote Sens.* **2019**, *11*, 2480. [CrossRef]

94. Zang, S.; Zhang, C.; Zhang, L.; Zhang, Y. Wetland remote sensing classification using support vector machine optimized with genetic algorithm: A case study in Honghe Nature National Reserve. *Sci. Geogr. Sin.* **2012**, *32*, 434–441.

95. Rodriguez-Galiano, V.F.; Ghimire, B.; Rogan, J.; Chica-Olmo, M.; Rigol-Sanchez, J.P. An assessment of the effectiveness of a random forest classifier for land-cover classification. *ISPRS J. Photogramm. Remote Sens.* **2012**, *67*, 93–104. [CrossRef]

96. Rousi, M.; Sitokonstantinou, V.; Meditskos, G.; Papoutsis, I.; Gialampoukidis, I.; Koukos, A.; Karathanassi, V.; Drivas, T.; Vrochidis, S.; Kontoes, C.; et al. Semantically enriched crop type classification and linked earth observation data to support the common agricultural policy monitoring. *IEEE J. Sel. Top. Appl. Earth Obs. Remote Sens.* **2020**, *14*, 529–552. [CrossRef]

97. Vreugdenhil, M.; Wagner, W.; Bauer-Marschallinger, B.; Pfeil, I.; Teubner, I.; Rüdiger, C.; Strauss, P. Sensitivity of Sentinel-1 backscatter to vegetation dynamics: An Austrian case study. *Remote Sens.* **2018**, *10*, 1396. [CrossRef]

98. Ainsworth, T.L.; Kelly, J.; Lee, J.S. Polarimetric analysis of dual polarimetric SAR imagery. In Proceedings of the 7th European Conference on Synthetic Aperture Radar, Friedrichshafen, Germany, 2–5 June 2008; pp. 1–4.

99. Moreira, A.; Prats-Iraola, P.; Younis, M.; Krieger, G.; Hajnsek, I.; Papathanassiou, K.P. A tutorial on synthetic aperture radar. *IEEE Geosci. Remote Sens. Mag.* **2013**, *1*, 6–43. [CrossRef]

100. Mandal, D.; Vaka, D.S.; Bhogapurapu, N.R.; Vanama, V.; Kumar, V.; Rao, Y.S.; Bhattacharya, A. Sentinel-1 SLC preprocessing workflow for polarimetric applications: A generic practice for generating dual-pol covariance matrix elements in SNAP S-1 toolbox. *Preprints* **2019**. [CrossRef]

101. Veci, L.; Lu, J.; Foumelis, M.; Engdahl, M. ESA's Multi-mission Sentinel-1 Toolbox. In Proceedings of the 19th EGU General Assembly, EGU2017, Vienna, Austria, 23–28 April 2017; p. 19398.

102. Schwerdt, M.; Schmidt, K.; Tous Ramon, N.; Klenk, P.; Yague-Martinez, N.; Prats-Iraola, P.; Zink, M.; Geudtner, D. Independent system calibration of Sentinel-1B. *Remote Sens.* **2017**, *9*, 511. [CrossRef]

103. Lee, J.S. Refined filtering of image noise using local statistics. *Comput. Graph. Image Process.* **1981**, *15*, 380–389. [CrossRef]

104. Filipponi, F. Sentinel-1 GRD preprocessing workflow. *Multidiscip. Digit. Publ. Inst. Proc.* **2019**, *18*, 11.

105. Drusch, M.; Del Bello, U.; Carlier, S.; Colin, O.; Fernandez, V.; Gascon, F.; Hoersch, B.; Isola, C.; Laberinti, P.; Martimort, P.; et al. Sentinel-2: ESA's optical high-resolution mission for GMES operational services. *Remote Sens. Environ.* **2012**, *120*, 25–36. [CrossRef]

106. Xue, J.; Su, B. Significant remote sensing vegetation indices: A review of developments and applications. *J. Sens.* **2017**, *2017*, 1353691. [CrossRef]

107. Sonobe, R.; Yamaya, Y.; Tani, H.; Wang, X.; Kobayashi, N.; Mochizuki, K.i. Crop classification from Sentinel-2-derived vegetation indices using ensemble learning. *J. Appl. Remote Sens.* **2018**, *12*, 026019. [CrossRef]

108. Hatfield, J.L.; Prueger, J.H. Value of using different vegetative indices to quantify agricultural crop characteristics at different growth stages under varying management practices. *Remote Sens.* **2010**, *2*, 562–578. [CrossRef]

109. Rouse, J.W., Jr.; Haas, R.H.; Schell, J.; Deering, D. *Monitoring the Vernal Advancement and Retrogradation (Green Wave Effect) of Natural Vegetation*; Contractor Report; NASA: Houston, TX, USA, 1973.

110. Verhegghen, A.; Bontemps, S.; Defourny, P. A global NDVI and EVI reference data set for land-surface phenology using 13 years of daily SPOT-VEGETATION observations. *Int. J. Remote Sens.* **2014**, *35*, 2440–2471. [CrossRef]

111. Asgarian, A.; Soffianian, A.; Pourmanafi, S. Crop type mapping in a highly fragmented and heterogeneous agricultural landscape: A case of central Iran using multi-temporal Landsat 8 imagery. *Comput. Electron. Agric.* **2016**, *127*, 531–540. [CrossRef]

112. Gao, B.C. NDWI—A normalized difference water index for remote sensing of vegetation liquid water from space. *Remote Sens. Environ.* **1996**, *58*, 257–266. [CrossRef]

113. Prajesh, P.; Kannan, B.; Pazhanivelan, S.; Ragunath, K. Monitoring and mapping of seasonal vegetation trend in Tamil Nadu using NDVI and NDWI imagery. *J. Appl. Nat. Sci.* **2019**, *11*, 54–61. [CrossRef]

114. Merzlyak, M.N.; Gitelson, A.A.; Chivkunova, O.B.; Rakitin, V.Y. Non-destructive optical detection of pigment changes during leaf senescence and fruit ripening. *Physiol. Plant.* **1999**, *106*, 135–141. [CrossRef]

115. Huete, A.R. A soil-adjusted vegetation index (SAVI). *Remote Sens. Environ.* **1988**, *25*, 295–309. [CrossRef]

116. Reed, B.C.; Schwartz, M.D.; Xiao, X. Remote sensing phenology. In *Phenology of Ecosystem Processes*; Springer: Berlin/Heidelberg, Germany, 2009; pp. 231–246.

117. Ok, A.O.; Akar, O.; Gungor, O. Evaluation of random forest method for agricultural crop classification. *Eur. J. Remote Sens.* **2012**, *45*, 421–432. [CrossRef]

118. Holland, J.H. *Adaptation in Natural and Artificial Systems: An Introductory Analysis with Applications to Biology, Control, and Artificial Intelligence*; MIT Press: Cambridge, MA, USA, 1992.

119. Hassanat, A.; Almohammadi, K.; Alkafaween, E.; Abunawas, E.; Hammouri, A.; Prasath, V. Choosing mutation and crossover ratios for genetic algorithms—A review with a new dynamic approach. *Information* **2019**, *10*, 390. [CrossRef]

120. Katoch, S.; Chauhan, S.S.; Kumar, V. A review on genetic algorithm: Past, present, and future. *Multimed. Tools Appl.* **2021**, *80*, 8091–8126. [CrossRef] [PubMed]

121. Mirjalili, S.; Song Dong, J.; Sadiq, A.S.; Faris, H. Genetic algorithm: Theory, literature review, and application in image reconstruction. In *Nature-Inspired Optimizers*; Studies in Computational Intelligence Book Series; Springer: Cham, Switzerland, 2020; Volume 811, pp. 69–85.

122. Roeva, O.; Fidanova, S.; Paprzycki, M. Population size influence on the genetic and ant algorithms performance in case of cultivation process modeling. In *Recent Advances in Computational Optimization*; Springer: Berlin/Heidelberg, Germany, 2015; pp. 107–120.

123. El Aboudi, N.; Benhlima, L. Review on wrapper feature selection approaches. In Proceedings of the 2016 International Conference on Engineering & MIS (ICEMIS), Agadir, Morocco, 22–24 September 2016; pp. 1–5.

124. Patil, V.; Pawar, D. The optimal crossover or mutation rates in genetic algorithm: A review. *Int. J. Appl. Eng. Technol.* **2015**, *5*, 38–41.

125. Sivanandam, S.; Deepa, S. *Introduction to Genetic Algorithms*; Springer: Berlin/Heidelberg, Germany, 2008.

126. Olympia, R.; Stefka, F.; Paprzycki, M. Influence of the Population Size on the Genetic Algorithm Performance in Case of Cultivation Process Modelling. In Proceedings of the 2013 Federated Conference on Computer Science and Information Systems, Krakow, Poland, 8–11 September 2013; pp. 371–376.

127. Suthaharan, S. Support vector machine. In *Machine Learning Models and Algorithms for Big Data Classification*; Springer: Berlin/Heidelberg, Germany, 2016; pp. 207–235.

128. Ndikumana, E.; Ho Tong Minh, D.; Baghdadi, N.; Courault, D.; Hossard, L. Deep recurrent neural network for agricultural classification using multitemporal SAR Sentinel-1 for Camargue, France. *Remote Sens.* **2018**, *10*, 1217. [CrossRef]

129. Flach, P. *Machine Learning: The Art and Science of Algorithms that Make Sense of Data*; Cambridge University Press: Cambridge, UK, 2012.

130. Maxwell, A.E.; Warner, T.A.; Fang, F. Implementation of machine-learning classification in remote sensing: An applied review. *Int. J. Remote Sens.* **2018**, *39*, 2784–2817. [CrossRef]

131. Géron, A. *Hands-On Machine Learning with Scikit-Learn, Keras, and TensorFlow: Concepts, Tools, and Techniques to Build Intelligent Systems*; O'Reilly Media, Inc.: Sebastopol, CA, USA, 2019.

132. Müller, A.C.; Guido, S. *Introduction to Machine Learning with Python: A Guide for Data Scientists*; O'Reilly Media, Inc.: Sebastopol, CA, USA, 2016.

133. Cervantes, J.; Garcia-Lamont, F.; Rodríguez-Mazahua, L.; Lopez, A. A comprehensive survey on support vector machine classification: Applications, challenges and trends. *Neurocomputing* **2020**, *408*, 189–215. [CrossRef]

134. Mountrakis, G.; Im, J.; Ogole, C. Support vector machines in remote sensing: A review. *ISPRS J. Photogramm. Remote Sens.* **2011**, *66*, 247–259. [CrossRef]

135. Ofori-Ampofo, S.; Pelletier, C.; Lang, S. Crop type mapping from optical and radar time series using attention-based deep learning. *Remote Sens.* **2021**, *13*, 4668. [CrossRef]

136. Zhong, L.; Hu, L.; Zhou, H. Deep learning based multi-temporal crop classification. *Remote Sens. Environ.* **2019**, *221*, 430–443. [CrossRef]

137. Vuolo, F.; Neuwirth, M.; Immitzer, M.; Atzberger, C.; Ng, W.T. How much does multi-temporal Sentinel-2 data improve crop type classification? *Int. J. Appl. Earth Obs. Geoinf.* **2018**, *72*, 122–130. [CrossRef]

138. Sun, Y.; Qin, Q.; Ren, H.; Zhang, T.; Chen, S. Red-edge band vegetation indices for leaf area index estimation from Sentinel-2/msi imagery. *IEEE Trans. Geosci. Remote Sens.* **2019**, *58*, 826–840. [CrossRef]

139. Kraskov, A.; Stögbauer, H.; Grassberger, P. Estimating mutual information. *Phys. Rev. E* **2004**, *69*, 066138. [CrossRef]

140. Ross, B.C. Mutual information between discrete and continuous data sets. *PLoS ONE* **2014**, *9*, e87357. [CrossRef]